J. Fluid Mech. (2023), *vol*. 962, A33, doi:10.1017/jfm.2023.310

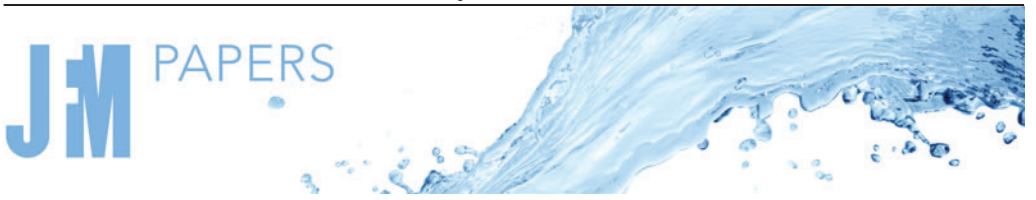

The catalytic effect of near-inertial waves on β-plane zonal jets

Lin-Fan Zhang[1] **and Jin-Han Xie**[1,2,†]

[1]Department of Mechanics and Engineering Science at College of Engineering, State Key Laboratory for Turbulence and Complex Systems, Beijing 100871, PR China

[2]Joint Laboratory of Marine Hydrodynamics and Ocean Engineering, Laoshan Laboratory, Shandong 266237, PR China

(Received 25 August 2022; revised 27 March 2023; accepted 2 April 2023)

Zonal jets and inertia–gravity waves are ubiquitous on planets such as Earth, Jupiter and Saturn. Motivated by the modification of energy flux of balanced flow by inertia–gravity waves, this paper studies the impact of near-inertial waves (NIWs) on zonal jets on a β-plane. Using a two-dimensional quasi-geostrophic and NIW coupled system on a β-plane (Xie & Vanneste, *J. Fluid Mech.*, vol. 774, 2015, pp. 143–169), we find NIWs catalytically impact several features of zonal jets. The NIWs inhibit jet formation due to the waves' catalytic induction of downscale mean energy flux. As the strength of NIWs increases, a critical point exists beyond which zonal jets are annihilated. The jet spacing is captured by the Rhines scale $L \sim \sqrt{U/\beta}$ with U estimated from the upscale energy flux induced by the mean flow alone, which again shows that the NIWs' impact is catalytic. Also, the temporal asymmetry of NIWs leads to the spatial asymmetry of jet dynamics. The jet profiles are asymmetric with a stronger shear on the left flank. And similar to the left turning of vortex dipole under the impact of NIWs, the NIW-modified jets migrate poleward. The NIWs also show a catalytic role in jet migration: the net momentum flux directly induced by NIWs is of secondary importance in the zonal mean momentum dynamics and impedes jet migration, while the advective effect of NIW-modified mean flow dominates the jet migration velocity.

Key words: quasi-geostrophic flows, waves in rotating fluids, geostrophic turbulence

1. Introduction

Rotation and stratification strongly impact geostrophic flows and lead to two distinctive motions: slow large-scale balanced flows and fast small-scale inertia–gravity waves (IGWs) (Smith & Waleffe 2002; Vallis 2006). The variation of the Coriolis effect with

† Email addresses for correspondence: jinhanxie@pku.edu.cn

latitude, the β-effect, leads to east–west flows with alternating directions, so-called zonal jets, which are ubiquitous on planets such as Jupiter, Saturn and Earth (Feldstein 1998; Sanchez-Lavega & Rojas 2000; García-Melendo 2001; Uppala *et al.* 2005). On Jupiter, the zonation of clouds shows the existence of jet streams (Vasavada & Showman 2005). On Earth, zonal jets play an important role in transporting energy, momentum and scalar quantities such as heat and salt, which impact the pattern of atmospheric and oceanic flows and living creatures (Rhines 1994). Nonlinear interactions between IGWs and mean flows have long been studied in geostrophic fluid dynamics (Lighthill 1978; Bühler 2009). Following this spirit, this paper focuses on the impact of IGWs on the formation, spacing, profile and dynamics of β-plane zonal jets.

Jet formation can be understood from turbulence phenomenology by matching the characteristic time scales of inverse cascade (Kraichnan 1967) and Rossby waves, whose anisotropic dispersion relation leads to an anisotropic barrier of upscale energy flux and favours jets (Vallis & Maltrud 1993). In a weakly nonlinear regime, Manfroi & Young (1999) showed that large-scale instability leads to the formation of slowly evolving jets. In a baroclinic model, Berloff, Kamenkovich & Pedlosky (2009) found that jets form through the secondary instability of the baroclinically unstable primary modes. From the points of the material conservation of potential vorticity, zonal jets arise inevitably because of the quasi-horizontal mixing of the background gradient of potential vorticity by nonlinear eddy motions over limited latitudinal regions (Dritschel & McIntyre 2008; Scott & Dritschel 2012; Galperin & Read 2019). In the quasi-linear approximation, where the inverse cascade is absent, the mechanisms of stochastic structural instability (Farrell & Ioannou 2003) and zonostrophic instability (Srinivasan & Young 2012) are proposed to explain jet formation.

What determines jet spacing is a long-lasting question. The Rhines scale (Rhines 1975) $L_{Rh} = \sqrt{U/\beta}$, where U is the root-mean-square (r.m.s.) velocity, is found to determine jet spacing in many circumstances (Williams 1978; Rhines 1979, 1994; Danilov & Gurarie 2000; Galperin *et al.* 2006; Chemke & Kaspi 2015*a*). Nevertheless, there is freedom in choosing the characteristic velocity U. For instance, Dritschel & McIntyre (2008) used the vortex-peak velocity and Scott & Dritschel (2012) calculated the r.m.s. velocity from the energy balance between the upscale energy flux of two-dimensional (2-D) turbulence and the frictional dissipation. Based on the characteristic scales of inverse cascade and Rossby wave, Maltrud & Vallis (1991) introduced the spectral Rhines scale, which describes the transition scale between turbulent and wavelike regimes. Dunkerton & Scott (2008) calculated the geometrical Rhines scale from the conservation of absolute angular momentum on a sphere for a jet's latitudinal spacing. However, the Rhines scale does not always predict the jet spacing when other characteristic scales such as the Rossby deformation radius L_D exist (Okuno & Masuda 2003; Smith 2004; Dritschel & McIntyre 2008).

Zonal jets have interesting asymmetric velocity profiles. García-Melendo (2001) and Sánchez-Lavega *et al.* (2008) observed asymmetric zonal jets on Jupiter, where the eastward jets form cusps at the maximum velocity while westward flows are smooth. This asymmetry is explained by the diagnostic relation between zonal velocity and potential vorticity staircases (Marcus & Lee 1998; Dritschel & McIntyre 2008). Woillez & Bouchet (2019) asymptotically derived the eastward zonal jets' velocity profile on a β-plane, and they showed that the potential vorticity staircase is an idealized approximation and the actual jet velocity profile is also controlled by the effects of friction, forcing and β. Lemasquerier, Favier & Le Bars (2021) experimentally found that zonal jets with a weak forcing can exist instantaneously even without the process of potential vorticity mixing.

Among the rich dynamics of zonal jets (cf. Galperin & Read 2019; Lemasquerier *et al.* 2021), one interesting phenomenon is their meridional migration. In the atmosphere, jets are found to migrate poleward in both observations (Riehl, Yeh & La Seur 1950; Dickey, Marcus & Hide 1992) and numerical simulations (James & Dodd 1996; Chemke & Kaspi 2015*b*), while jets' equatorward migration was observed in ocean models (Chan, Plumb & Cerovecki 2007; Ashkenazy & Tziperman 2016). Using a semi-hemisphere zonally re-entrant ocean model, Chan *et al.* (2007) found the primary jet oscillates meridionally and inconspicuously propagates poleward over a short range, and the secondary jets systematically migrate equatorward slowly from high latitudes and eventually merge with the primary jet. Besides, Williams (2003) described a similar equatorward jet migration in a model of Jupiter's atmosphere. Apart from gradual migration, abrupt jet transitions are also observed in forced-dissipative 2-D quasi-geostrophic (QG) systems (Bouchet & Venaille 2012; Rolland & Simonnet 2015; Bouchet, Marston & Tangarife 2018; Bouchet, Rolland & Simonnet 2019).

Among the wide range of frequency of IGWs, near-inertial waves (NIWs) contain around 50 % of the total wave energy in the ocean (Fu 1981; Ferrari & Wunsch 2009); therefore, we pay special attention to the effects of NIWs on zonal jets in this paper. The interaction between NIWs and balanced flow is twofold. When propagating in balanced flows, NIWs are affected by advection, refraction and dispersion, and they are trapped by anticyclones of balanced flow (Kunze, Schmitt & Toole 1995; Elipot, Lumpkin & Prieto 2010; Joyce *et al.* 2013; Thomas *et al.* 2020). Because the negative vorticity shifts the lower bound of the internal waveband to a frequency slightly below the Coriolis frequency f, NIWs with frequency less than f concentrate in anticyclones (Kunze 1985). The NIWs trapped in anticyclones are also found to propagate downward to the deeper ocean, which is called the inertial chimney phenomenon (Lee & Niiler 1998). Considering the comparable horizontal scales of NIWs and balanced flow, Young & Ben Jelloul (1997) asymptotically derived an amplitude equation (YBJ equation) of first-order accuracy in the Burger number of the NIWs. Asselin & Young (2019) further proposed the YBJ$^+$ equation, which captures the second-order effect of the linear dispersion relation of IGWs. Danioux, Vanneste & Bühler (2015) applied the YBJ model to explain the concentration of NIWs in anticyclones based on conserved quantities. Using the three-dimensional YBJ equation, Asselin *et al.* (2020) studied the weakly dispersive NIWs' wavevector impacted by refraction and strain, which is justified by observation (Thomas *et al.* 2020).

With large horizontal and small vertical scales, NIWs are weakly dispersive and potentially have a strong impact on the balanced flow. With $O(1)$ Rossby number, Gertz & Straub (2009) and Taylor & Straub (2016) numerically found that NIWs provide an effective energy sink for wind-driven ocean gyres. Spontaneous generation of IGWs (cf. Vanneste (2013), and references therein) is thought to be important for energy sink for the balanced flow, which is exponentially weak in the regime of small Rossby number (Vanneste 2008), and it can be effective when the Rossby number is of $O(1)$, which was shown in numerical simulations (Danioux *et al.* 2012; Plougonven & Snyder 2007) and by analytical solutions (Zeitlin 2008; Thomas 2012; Whitt & Thomas 2015; Grisouard & Thomas 2016). However, the strength of the NIW sink may be overestimated, as a considerable amount of wave energy can be reabsorbed by the mean flow (Nagai *et al.* 2015; Shakespeare & McC. Hogg 2018). Stimulated loss of balance (Xie & Vanneste 2015; Wagner & Young 2016; Rocha, Wagner & Young 2018) is also proposed as a mechanism to absorb energy from balanced flow by NIWs. Based on a generalized Lagrangian mean framework (Andrews & Mcintyre 1978; Soward & Roberts 2010; Salmon 2013), this mechanism implies that the decrease of NIW horizontal scale by mean-flow advection and

refraction leads to energy conversion from balanced motions to NIWs. Weakened balanced flows, in turn, enfeeble wave refraction and thus halt the drainage of waves into the interior ocean (Asselin & Young 2020). Using the coupled QG–YBJ model (Xie & Vanneste 2015) with initially uniform NIWs, Kafiabad, Vanneste & Young (2021) calculated the NIW frequency shift that is linearly proportional to wave kinetic energy.

The presence of NIWs also catalyses other processes in mean flows. With linear analytical solutions, Thomas (2012) found that IGWs play a catalytic role when fronts lose balance to ageostrophic motions in frontogenesis. By analysing frequency-space filtered numerical data, Barkan, Winters & McWilliams (2017) and Barkan *et al.* (2021) found that NIWs catalyse energy transfer from mesoscale to submesoscale. By studying a Galerkin-truncated 2-D model of rotating stratified flow, Thomas & Arun (2020) found that high-energy NIWs can transfer energy to barotropic flow and impel a forward energy cascade of the balanced flows that assists the forward energy cascade of waves in turn. By studying a 2-D model derived asymptotically in Xie & Vanneste (2015), in statistically steady states with external forcing and dissipation, Xie (2020) proposed that based on the conservations of energy, wave action and potential enstrophy, NIWs catalyse a downscale energy transfer of QG mean flows.

This paper studies the impact of NIWs on jet dynamics on a β-plane, which is motivated by ubiquitous waves and jets and the impact of NIWs on the energy flux of mean flows. The rest of this paper is organized as follows. In § 2, we first present the coupled model of QG mean flows and NIWs following Xie & Vanneste (2015). In § 3, we show the impact of NIWs on the energy evolution, the energy spectra of mean flow and NIWs and qualitatively analyse the catalytic effect of NIWs from the perspective of the mean-flow energy flux. In § 4, we quantitatively study the impact of NIWs on jet formation and find that NIWs weaken jets. In § 5, we study the dependence of jet spacing on NIW strength. A modified Rhines scale estimated using the advective upscale mean energy flux alone captures the jet spacing well. This indirect impact of NIWs again shows a catalytic effect. In § 6, we find that NIWs break jets' spatial symmetry by introducing asymmetric jet flank and leading to jets' poleward migration. In studying the jet migration from the mean momentum balance, the NIWs' direct impact is much weaker than that of the asymmetric mean flow, which shows the third NIW catalytic effect. Finally, in § 7, we summarize and discuss our results.

2. Coupled model of NIW–mean flow interaction on a β-plane

For simplicity and numerical efficiency and to capture the key feature of wave–mean flow interaction, we study the interaction between a single-vertical-mode NIW and a barotropic QG mean flow using the 2-D model derived by Xie & Vanneste (2015) on a β-plane:

$$\partial_t q + J(\psi, q) = 0, \tag{2.1a}$$

$$\partial_t \phi + J(\psi, \phi) + \mathrm{i} g(y)\phi - \frac{\mathrm{i} f_0}{2} L^2 \phi + \frac{\mathrm{i}}{2} \nabla^2 \psi \phi = 0, \tag{2.1b}$$

where

$$q = \nabla^2 \psi + g(y) + \frac{\mathrm{i} f_0}{2} J(\phi^*, \phi) + \frac{f_0}{4} \nabla^2 |\phi|^2 \tag{2.2}$$

is the NIW-modified quasi-geostrophic potential vorticity (QGPV). Here, ψ is the Lagrangian mean streamfunction and the horizontal velocity of QG mean flows is $(u, v) = (-\partial_y \psi, \partial_x \psi)$; $f_0 = \text{const.}$ is the local Coriolis frequency; and ϕ is the complex wave amplitude and links to the two horizontal velocities (u_0, v_0) through

$u_0 + \mathrm{i}v_0 = -\mathrm{i}f_0\phi\,\mathrm{e}^{-\mathrm{i}f_0 t+\mathrm{i}mz}$ with m the vertical wavenumber of the single-vertical-mode NIW. The asterisk denotes the complex conjugate and $J(a,b) = a_x b_y - a_y b_x$ is the Jacobian. Also, $g(y)$ is the variation of the Coriolis parameter f in the meridional direction such that $f = f_0 + g(y)$; therefore, the β-effect is captured by $\beta = \partial_y g$. This model consists of the equation describing the material-invariant QGPV (2.1*a*) and the linear equation capturing the slow modulation of NIW amplitude (Young & Ben Jelloul 1997). In (2.1*b*) we consider a modified dispersion (Asselin & Young 2019) with the operator

$$L^2 = \frac{\nabla^2}{\dfrac{f_0^2}{N^2}m^2 - \dfrac{1}{4}\nabla^2}, \tag{2.3}$$

where N is the buoyancy frequency. Here, the Laplacian operator in the denominator should be understood in the spectral space. This modified dispersion term captures the high-order corrections of the NIW dispersion relation and improves the numerical efficiency by bounding the frequency as the wavenumber increases.

For simplicity, we introduce a modified meridional-dependent β-effect, $\beta(y)$, which is periodic in y instead of the traditional choice of a constant, to perform numerical simulations in a periodic domain. Practically, to extend the region with a constant β, we prescribe

$$\beta(y) = \begin{cases} \beta_0 \dfrac{\mathrm{e}^{l_b y} - \mathrm{e}^{-l_b y}}{\mathrm{e}^{l_b y} + \mathrm{e}^{-l_b y}}, & 0 \le y < L_y/4, \\ \beta_0 \dfrac{\mathrm{e}^{l_b (L_y/2-y)} - \mathrm{e}^{-l_b (L_y/2-y)}}{\mathrm{e}^{l_b (L_y/2-y)} + \mathrm{e}^{-l_b (L_y/2-y)}}, & L_y/4 \le y < 3L_y/4, \\ \beta_0 \dfrac{\mathrm{e}^{l_b (-L_y+y)} - \mathrm{e}^{-l_b (-L_y+y)}}{\mathrm{e}^{l_b (-L_y+y)} + \mathrm{e}^{-l_b (-L_y+y)}}, & 3L_y/4 \le y < L_y, \end{cases} \tag{2.4}$$

where $\beta_0 = \text{const.}$, l_b is a constant that controls the range of the variation in β and L_y is the domain size in the meridional direction. Our analysis uses the data obtained from the region $\approx [1/l_b, L_y/2 - 1/l_b]$, where β is almost a constant. The other half of the domain is only introduced for numerical simulation, and it is unphysical because β should be positive in the northern hemisphere. We use the current periodic set-up mainly because of its simplicity and computational efficiency. The expressions of $\beta(y)$ and $g(y)$ are illustrated in figure 1. An alternative set-up is to consider a constant-β system in a channel, which is widely used. For example, Abernathey, Marshall & Ferreira (2011) numerically simulated a β-plane channel with a sponge layer at the northern boundary to study the Antarctic Circumpolar Current.

The coupled system (2.1) conserves energy, potential enstrophy and wave action, which reads

$$\mathcal{E} = \int \left\{ \underbrace{\frac{1}{2}|\nabla\psi|^2}_{\mathcal{E}_{QG}} + \underbrace{\frac{1}{2}f_0 g(y)|\phi|^2}_{\mathcal{E}_\beta} + \underbrace{\frac{f_0^2}{4}|L\phi|^2}_{\mathcal{E}_{NIW}} \right\} \mathrm{d}\boldsymbol{x}, \tag{2.5a}$$

$$\mathcal{P} = \int q^2\,\mathrm{d}\boldsymbol{x}, \tag{2.5b}$$

$$\mathcal{A} = \int |\phi|^2\,\mathrm{d}\boldsymbol{x}. \tag{2.5c}$$

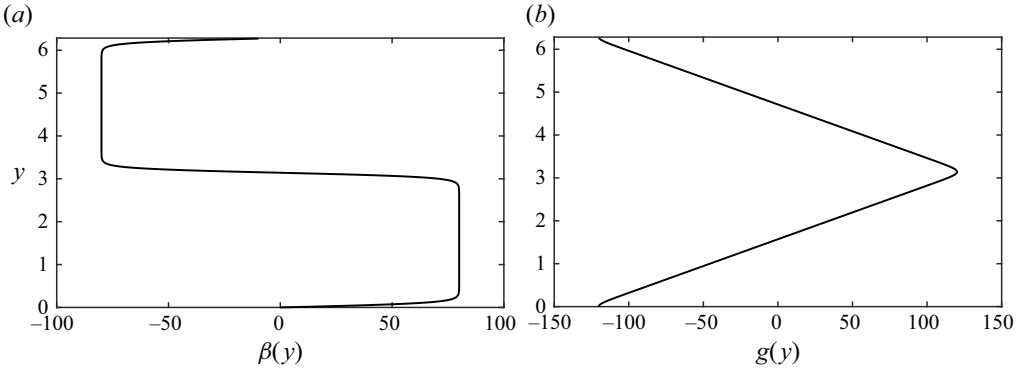

Figure 1. Illustration of (*a*) $\beta(y)$ and (*b*) $g(y)$ with $L_y = 2\pi$ and $l_b = 10$ in (2.4).

Here we decompose the total energy into three components corresponding to the mean, β-effect and wave potential energy for convenience of later discussion.

In this paper, we focus on the statistically steady states of the NIW–mean flow coupled system with external forcing and dissipation. Following Xie (2020), for a straightforward quantification of energy injection rate to the mean and wave components, forcing and dissipation are added to the mean vorticity equation instead of the QGPV equation and the wave amplitude equation. Therefore we obtain the system

$$\partial_t \nabla^2 \psi + \mathcal{N}(\psi, \phi) = D_1 \nabla^2 \psi + M_F k_f^{1/2} \mathsf{F}_1, \tag{2.6a}$$

$$\partial_t \phi + J(\psi, \phi) + \mathrm{i} g(y)\phi - \frac{\mathrm{i} f_0}{2} L^2 \phi + \frac{\mathrm{i}}{2} \nabla^2 \psi \phi = D_2 \phi + R M_F \frac{m}{2 N k_f^{3/2}} \mathsf{F}_2, \tag{2.6b}$$

where the artificial dissipation operators take the form of $D_1 = -\alpha_1 + \nu_1 \nabla^6$ and $D_2 = \alpha_2 \nabla^{-2} + \nu_2 \nabla^6$ with constants α_i and ν_i $(i = 1, 2)$. The external forcings F_i $(i = 1, 2)$, which are white-noise in time, are isotropic in space and centre around wavenumber $|\boldsymbol{k}| = k_f$, where $\boldsymbol{k} = (k, l)$ is the 2-D wavenumber vector in spectral space. Therefore,

$$\langle \mathsf{F}_i(\boldsymbol{x}_1, t_1) \mathsf{F}_i(\boldsymbol{x}_2, t_2) \rangle = C_0 J_0(k_f |\boldsymbol{x_1} - \boldsymbol{x_2}|) \delta(t_1 - t_2), \tag{2.7}$$

where $\langle \cdot \rangle$ is an ensemble average, C_0 is the covariance and J_0 is the zeroth-order Bessel function. Here M_F and R control the external forcing magnitude and $k_f^{1/2}$ and $m/(N k_f^{3/2})$ are the normalized coefficients. Combining (2.5*a*) and (2.6), we estimate the energy injection rates of QG mean flow and NIW as $\epsilon_{QG} \sim M_F^2/2$ and $\epsilon_{NIW} \sim R^2 M_F^2 f_0^2 m^2/(16 f_0^2 m^2 + 4 N^2 k_f^2)$. Therefore, we define the ratio between energy injection rates of NIW and mean flow as

$$\lambda = \frac{R^2 m^2 f_0^2}{8 m^2 f_0^2 + 2 N^2 k_f^2}. \tag{2.8}$$

Here, the denominator is consistent with the modification by Asselin & Young (2019), and when this modification is absent, $\lambda = R^2/8$.

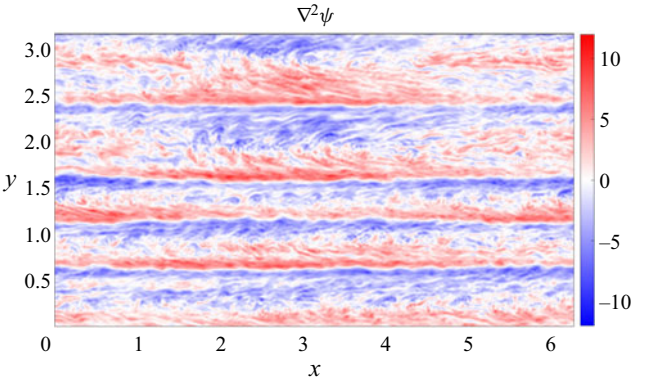

Figure 2. A snapshot of QG mean flow vorticity fields in the statistically steady state of the NIW-free simulation with $\epsilon_{QG} = 8 \times 10^{-5}$.

We decompose the nonlinear term $\mathcal{N}(\psi, \phi)$ in (2.6*a*) into different components for convenience in later discussions as

$$\mathcal{N}(\psi, \phi) = \mathcal{N}_\beta(\psi) + \mathcal{N}_m(\psi) + \mathcal{N}_W(\psi, \phi), \tag{2.9}$$

where

$$\mathcal{N}_\beta(\psi) = g_y \psi_x + \frac{f_0}{2} g_y(\phi_x^* \phi + \phi^* \phi_x), \tag{2.10a}$$

$$\mathcal{N}_m(\psi) = J(\psi, \nabla^2 \psi), \tag{2.10b}$$

$$\mathcal{N}_W(\psi, \phi) = \frac{-f_0^2}{4}(J(\phi^*, L^2\phi) - J(L^2\phi^*, \phi)) - \frac{\mathrm{i} f_0^2}{8}\nabla^2(\phi L^2\phi^* - \phi^* L^2\phi)$$
$$-\frac{f_0}{2}\nabla \cdot J(\nabla\psi, |\phi|^2). \tag{2.10c}$$

3. Basic properties of the NIW–QG coupled system on a β-plane

We run the numerical simulations using a Fourier pseudospectral method with 2/3 dealiasing in space and a resolution of 512×512 in a domain size of $2\pi \times 2\pi$. We apply a fourth-order explicit Runge–Kutta temporal scheme (cf. Cox & Matthews 2002) where the linear terms are solved by an integrating factor method, and the nonlinear terms are explicitly approximated. We choose $\beta_0 = 80$ and $f_0 m/N = 32$ in all simulations. The QG mean flows and NIWs are driven by external forcing at a forcing wavenumber $k_f = 32$. We vary two parameters M_F and R to create a matrix of results. Thus, the energy injection rates are $\epsilon_{QG} = 8 \times 10^{-5}, 3.2 \times 10^{-4}, 7.2 \times 10^{-4}$ with $M_F = 1000, 2000, 3000$. Parameter R ranges from 0 to 3.6, and the energy injection ratio of NIWs to mean flows λ varies from 0 to 1.296 by (2.8).

We first run numerical simulations without NIWs as references to study the wave effect. Figure 2 shows a snapshot of the vorticity field $\nabla^2\psi$ of a NIW-free simulation with $\epsilon_{QG} = 8 \times 10^{-5}$ at a statistically steady state when jets form. Then we use this vorticity field as the initial condition for other NIW-involved simulations with non-zero λ.

In this section, we focus on qualitative descriptions of characteristic features and leave quantitative studies to §§ 4–6.

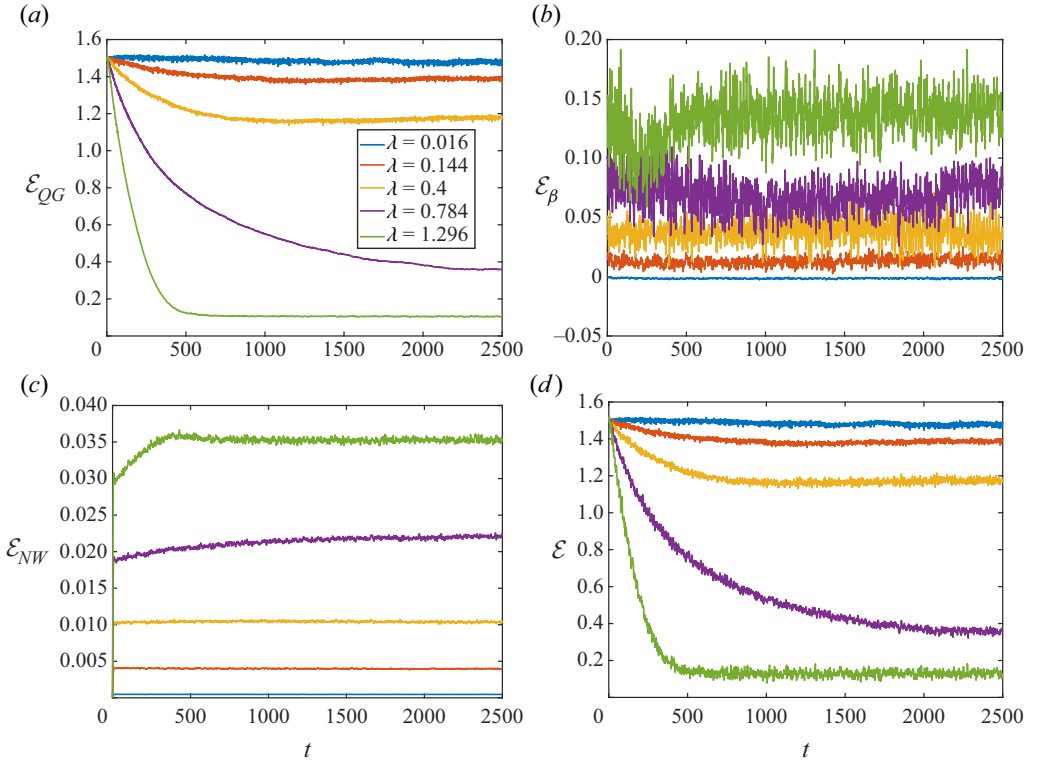

Figure 3. Evolutions of (*a*) QG mean, (*b*) β-related, (*c*) NIW and (*d*) total energy (cf. (2.5*a*)) in simulations with $\lambda = 0.016, 0.144, 0.4, 0.784, 1.296$. In (*b*), for clarity we vertically shift the curves following $\mathcal{E}_\beta(\lambda = 0.144) + 0.02$, $\mathcal{E}_\beta(\lambda = 0.4) + 0.05$, $\mathcal{E}_\beta(\lambda = 0.784) + 0.1$, $\mathcal{E}_\beta(\lambda = 1.296) + 0.15$. The legend in (*a*) applies to all four panels.

3.1. *Energy evolution and statistically steady states*

In this subsection, we run the coupled system into statistically steady states. We display NIWs' impact on the total, wave and mean energy evolution. Figure 3(*a*) shows the evolution of mean energy with different energy injection ratios λ. When NIWs are injected, the mean energy $\mathcal{E}_{QG}$ decreases and gradually reaches a statistically steady state. With a stronger NIW energy injection rate, the steady value of $\mathcal{E}_{QG}$ becomes weaker, and the relaxation time to reach the statistically steady states increases and then decreases. This non-monotonic dependence implies the existence of a phase transition associated with the disappearance of the jet (cf. figure 4*d*). In figure 3(*b*), the β-related NIW energy, $\mathcal{E}_\beta$, oscillates around zero and the amplitude of oscillation increases as λ increases. Compared with $\mathcal{E}_{QG}$, $\mathcal{E}_\beta$ is relatively small. Figure 3(*c*) shows that the evolution of wave potential energy $\mathcal{E}_{NIW}$ has three stages. First, there is a sudden wave energy adjustment at a short time interval, then the wave energy increases in a comparable time scale to the mean energy changes and, finally, a statistically steady state is reached. Since $\mathcal{E}_\beta$ and $\mathcal{E}_{NIW}$ are small compared with $\mathcal{E}_{QG}$, figure 3(*d*) shows that the total energy $\mathcal{E}$ is dominated by $\mathcal{E}_{QG}$ but with stronger fluctuations.

Snapshots of statistically steady QG mean flow vorticity field $\nabla^2\psi$ are presented in figure 4. When the energy injection rate of NIWs is weak (figure 4*a* with $\lambda = 0.144$), zonal jets remain similar in magnitude and shape compared with those in the

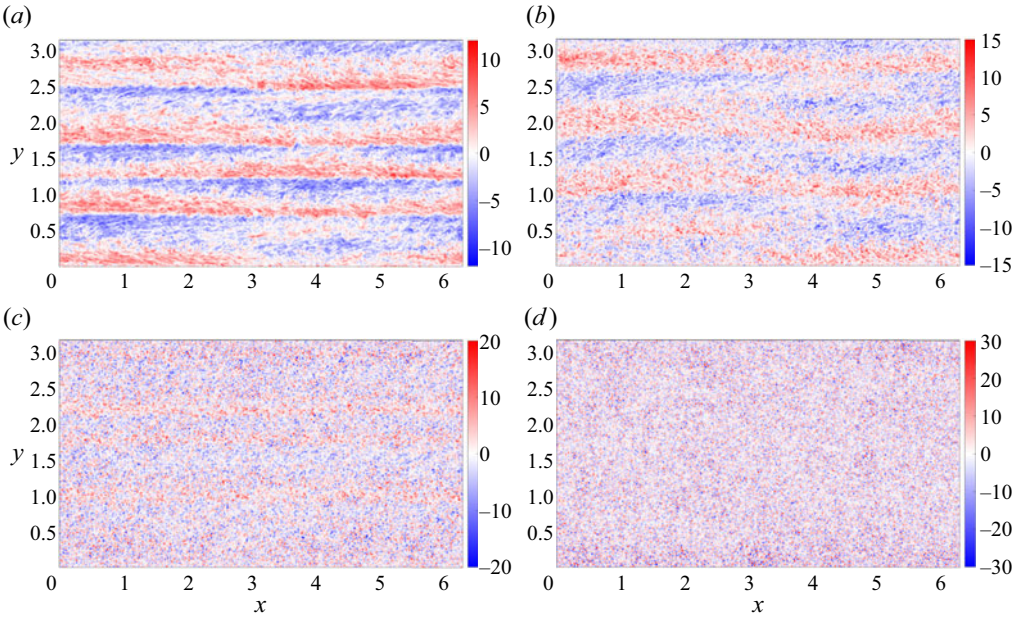

Figure 4. Snapshots of QG mean vorticity fields, $\nabla^2\psi$, at statistically steady states with (*a*) $\lambda = 0.144$, (*b*) $\lambda = 0.4$, (*c*) $\lambda = 0.784$ and (*d*) $\lambda = 1.296$. The mean energy injection rate is $\epsilon_{QG} = 8 \times 10^{-5}$.

NIW-free case. As the energy injection ratio of NIW to mean flows increases ($\lambda = 0.4$ and 0.784 shown in figures 4*b* and 4*c*), jets weaken and the jet spacing increases. When the energy injection ratio is large enough (figure 4*d* with $\lambda = 1.296$), jets disappear. Compared with the vorticity field without NIWs in figure 2, zonal jets are weakened by NIWs and their geometries are modified, which we study quantitatively in §§ 4–6.

3.2. *Energy spectra*

To present the impact of NIWs on the spectrum of QG mean flow and, in particular, the jets, based on the 2-D energy spectrum

$$E(\boldsymbol{k}) = \frac{1}{2}|\boldsymbol{k}|^2\hat{\psi}(\boldsymbol{k})\hat{\psi}^*(\boldsymbol{k}), \tag{3.1}$$

where the hat $\hat{\cdot}$ denotes the Fourier transform, we define the one-dimensional spectra of the total mean energy, the jet energy and the perturbation energy as

$$E_T(K) = \sum_{|\boldsymbol{k}|=K-1/2}^{K+1/2} E(\boldsymbol{k}), \tag{3.2a}$$

$$E_Z(K) = \sum_{|\boldsymbol{k}|=K-1/2}^{K+1/2} E(0, l), \tag{3.2b}$$

$$E_R(K) = \sum_{|\boldsymbol{k}|=K-1/2}^{K+1/2} E(k \neq 0, l). \tag{3.2c}$$

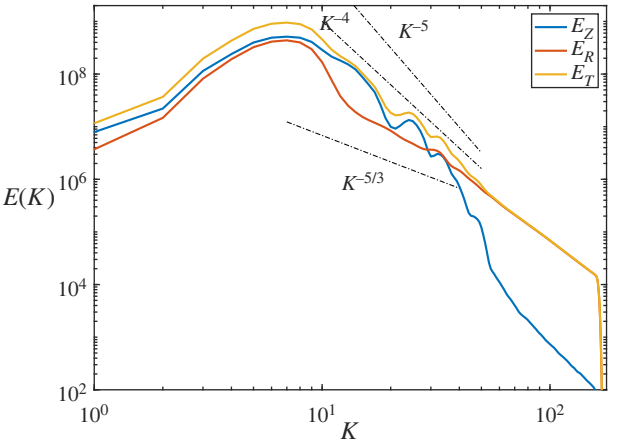

Figure 5. The QG mean energy spectrum without NIWs at a statistically steady state with $\epsilon_{QG} = 8 \times 10^{-5}$.

Here, $E_T(K) = E_Z(K) + E_R(K)$. In the classic 2-D β-plane turbulence, the jet and perturbation energy spectra follow the scalings $E_Z(K) = C_Z\beta^2K^{-5}$ and $E_R(K) = C_K\epsilon^{2/3}K^{-5/3}$, where ϵ is the viscous dissipation rate (Galperin, Sukoriansky & Dikovskaya 2010). The 2-D potential energy spectrum of NIWs is defined as

$$E_W(K) = \frac{f_0^2}{4} \sum_{|\boldsymbol{k}|=K-1/2}^{K+1/2} \widehat{L\phi}(\boldsymbol{k})\widehat{L\phi}^*(\boldsymbol{k}). \tag{3.3}$$

First, we show the spectra of the statistically steady state in the NIW-free simulation in figure 5. At scales between the spectral peak and the forcing wavenumber, the mean and perturbation energy spectra follow $K^{-5/3}$ and K^{-4} scalings, respectively. This K^{-4} scaling was derived by Danilov & Gurarie (2004) with consideration of a sawtooth profile of zonal mean vorticity, making it different from the classic K^{-5} scaling proposed by Rhines (1975). To show the wave effect, we present energy spectra with different energy injection ratios λ in figure 6. From figure 6(a), we find that as λ increases from 0 to 1.024, the peaks of $E_Z(K)$ move to smaller wavenumber; in the intermediate scale between spectral peak and the energy injection scale, the jet energy drops but keeps the K^{-4} scaling. However, when $\lambda = 1.296$, jets disappear and $E_Z(K)$ deviates from the classic K^{-5} scaling. Figure 6(b) shows that as the NIW energy injection rate gradually becomes comparable with the mean energy injection rate, the perturbation energy drops at the large scale and increases at the small scale; the peak of $E_R(K)$ also moves to larger wavenumbers; and the range of the perturbation energy spectrum with the $K^{-5/3}$ scaling shortens and finally disappears. When jets completely disappear with $\lambda = 1.296$, for wavenumbers smaller than k_f, $E_R(K)$ follows a K scaling. The combination of jet and perturbation energy spectra, $E_Z(K)$ and $E_R(K)$, respectively, explains the variation of total energy spectrum scaling from K^{-4} to $K^{-5/3}$ and finally to K under the influence of increasing energy injection ratio λ, which is shown in figure 6(c). However, when the NIW energy injection rate is large enough, such as $\lambda = 1.296$, figures 6(a)–6(c) show that at scales between the spectral peak and the forcing wavenumber, the jet and perturbation spectra differ from the scalings in the theories without wave impact. As to the potential energy spectrum of NIWs in figure 6(d), as the energy injection ratio λ increases, for wavenumbers smaller than the forcing wavenumber, it reaches its largest value when $\lambda = 1.024$, corresponding to jet disappearance. If we

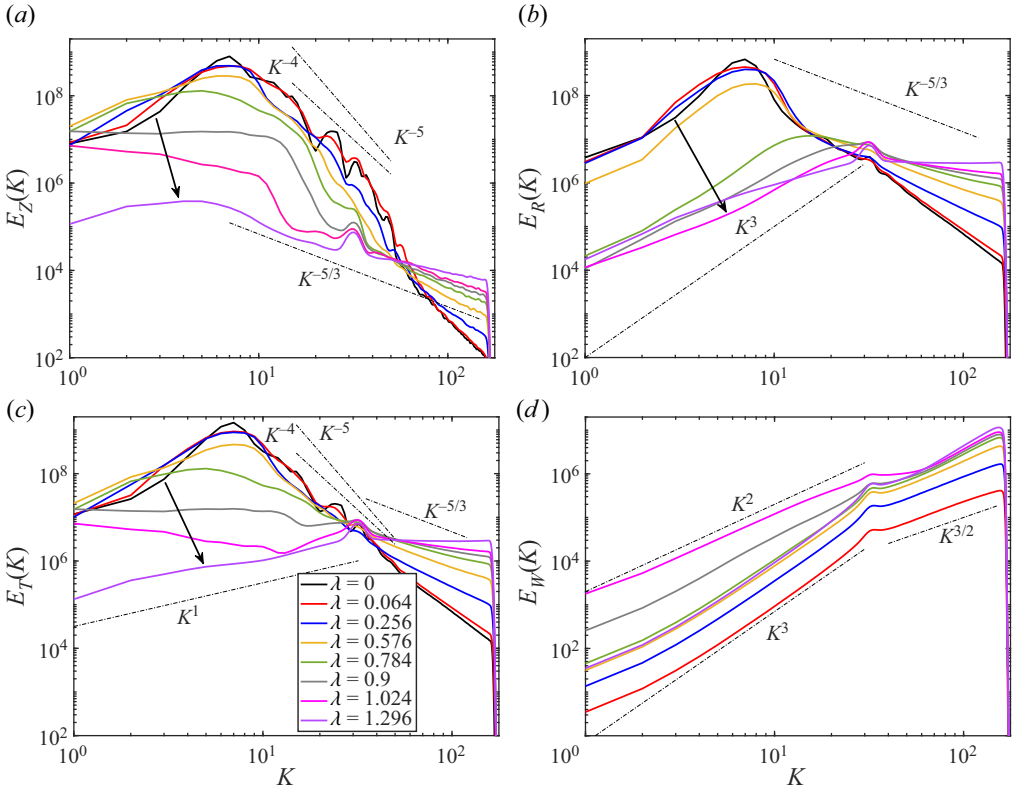

Figure 6. The NIW-modified QG mean and NIW energy spectra at statistically steady states with λ ranging from 0 to 1.296: (*a*) $E_Z(K)$, (*b*) $E_R(K)$, (*c*) $E_T(K)$ and (*d*) $E_W(K)$. The legend in (*c*) applies to all four panels. The black dash-dotted lines are power functions for reference. The black arrows show the direction of increasing λ.

treat the jet strength as an order parameter and the NIW as a perturbation, the increase in perturbation strength implies the existence of a phase transition, which we study in § 4.

3.3. *Energy flux across scales*

Since the energy flux of the QG mean flows across scales relates to jet formation (Rhines 1975; Vallis & Maltrud 1993; Chekhlov *et al.* 1996; Sukoriansky, Dikovskaya & Galperin 2007), this subsection focuses on the QG mean energy flux influenced by NIWs to explain jet weakening and annihilation observed in vorticity fields and mean energy spectra. The spectral energy flux of QG mean flow is defined as

$$F_{QG}(K) = \sum_{|\boldsymbol{k}|=0}^{K} \frac{-|\boldsymbol{k}|^2}{2}(\hat{\psi}\hat{\mathcal{N}}^* + \text{c.c.}), \tag{3.4}$$

and the positive and negative values of F_{QG} correspond to downscale and upscale fluxes, respectively.

To show the influence of mean flow and NIWs separately, we decompose the energy flux of mean flow as follows:

$$F_{QG} = F_{QG}^{m} + F_{QG}^{NIW}, \quad \text{with} \tag{3.5a}$$

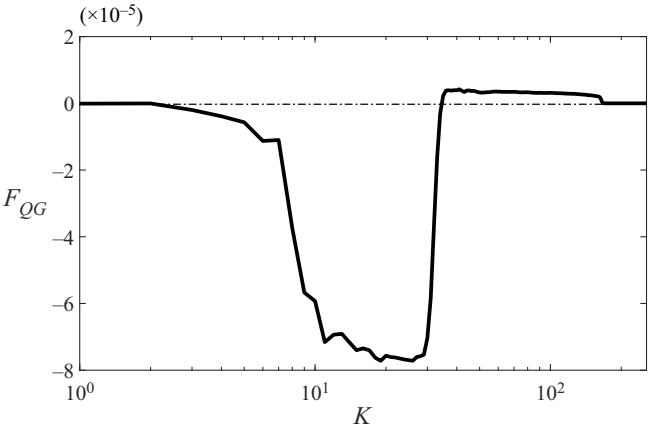

Figure 7. The QG mean energy flux without NIWs at a statistically steady state with $k_f = 32$ and $\epsilon_{QG} = 8 \times 10^{-5}$. The negative and positive values denote the upscale and downscale energy fluxes, respectively.

$$F^m_{QG} = \sum_{|\boldsymbol{k}|=0}^{K} \frac{1}{2}(\hat{\psi}\hat{\mathcal{N}}^*_m + \text{c.c.}), \tag{3.5b}$$

$$F^{NIW}_{QG} = \sum_{|\boldsymbol{k}|=0}^{K} \frac{1}{2}(\hat{\psi}\hat{\mathcal{N}}^*_{NIW} + \text{c.c.}), \tag{3.5c}$$

where the superscripts 'm' and 'NIW' denote the effects of mean flow and NIWs, respectively.

When NIWs are absent, the coupled system (2.1) is identical to the 2-D turbulence system on a β-plane; therefore, the mean energy should transfer upscale with a constant value, which is shown in figure 7. Here, the finite hyperviscosity brings about a weak downscale flux.

In figure 8 we present the energy flux of mean flow with different energy injection rates of NIWs. The NIWs induce bidirectional flux of mean-flow energy, and as λ increases, the portion of downscale flux increases, as shown in figures 8(a)–8(c). Therein, both the energy flux induced by mean flow, F^m_{QG}, and the energy flux induced by NIWs, F^{NIW}_{QG}, increase and the cancellation of these two parts leaves a bidirectional mean-flow energy flux. When λ is large enough (cf. figure 8d), all the mean energy transfers downscale. The presence of mean-flow inertial ranges with constant energy fluxes above and below the forcing wavenumber implies negligible conversion between QG mean flow and NIWs, which is consistent with the catalytic effect of NIWs on the mean energy flux (Xie 2020; Barkan *et al.* 2021).

4. Dependence of jet magnitude on the strength of NIWs

In this section, we study the dependence of jet strength on the strength of NIWs, which λ parametrizes. We define jet energy as $\mathcal{E}_{jet} = \int \bar{u}^2/2 \, \mathrm{d}\boldsymbol{x}$, where $\bar{u}$ is the zonal-averaged zonal QG mean velocity. Figure 9(a) shows the dependence of $\mathcal{E}_{jet}/\mathcal{E}_{QG}$ on λ at statistically steady states with different mean energy injection rates. When the mean energy injection rate, ϵ_{QG}, is fixed, there exists a critical value λ_c: when $0 < \lambda < \lambda_c$, $\mathcal{E}_{jet}/\mathcal{E}_{QG}$ is almost a constant, and when λ goes across the critical points λ_c, it abruptly drops to a value

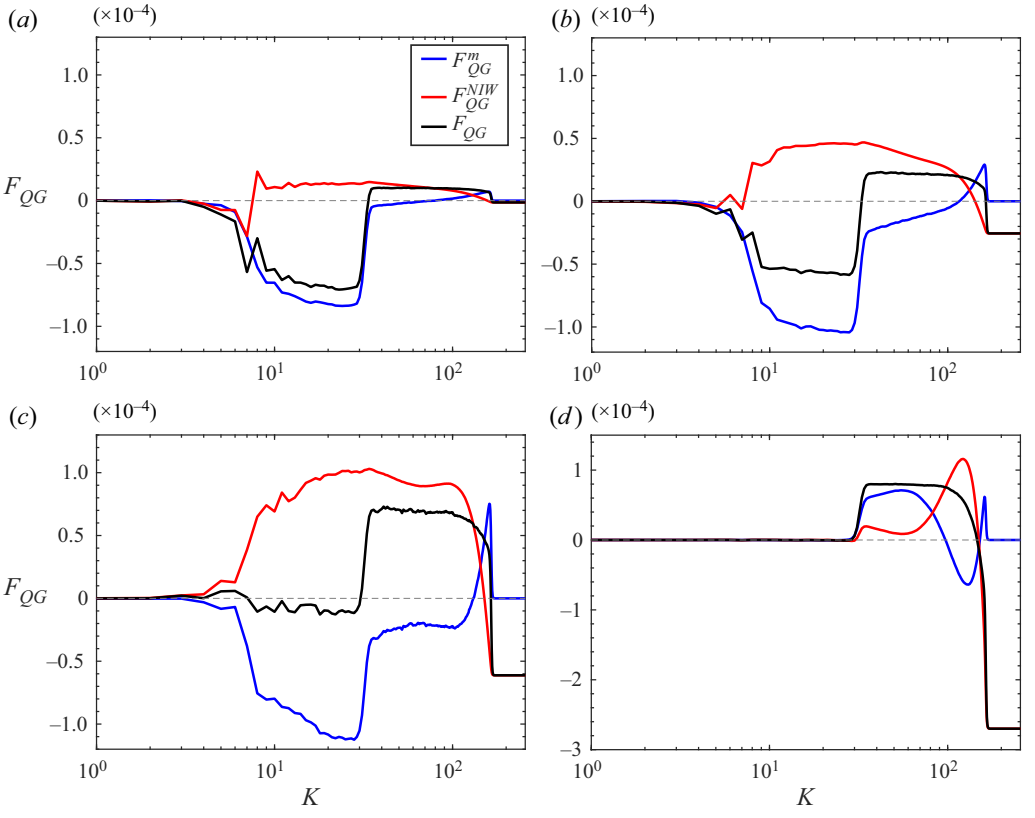

Figure 8. Energy flux of QG mean flow in NIW-containing cases of (*a*) $\lambda = 0.144$, (*b*) $\lambda = 0.4$, (*c*) $\lambda = 0.784$ and (*c*) $\lambda = 1.296$ with $k_f = 32$ and $\epsilon_{QG} = 8 \times 10^{-5}$.

close to 0. Therefore, as the NIW energy injection rate increases from 0, the QG–NIW coupled system experiences a first-order phase transition, across which jets suddenly disappear.

Next, we explore the dependence of QG mean energy injection rate ϵ_{QG} on critical values λ_c. Since near the critical point the jet magnitude is small, in the mean vorticity equation (2.6*a*), by ignoring the mean-flow impact, we obtain the quasilinear balance between nonlinear wave term in (2.10*c*) and the external forcing, i.e. $\mathcal{N}_W \sim M_F k_f^{1/2} \mathsf{F}_1$, leading to $|\phi|^2 \sim M_F k_f^{-1/2} f_0^{-2}$. The wave magnitude can be estimated by $|\phi| \sim R M_F m N^{-1} f_0^{-1} k_f^{-3/2}$ from the wave equation (2.6*b*). Combining them we obtain $R^2 \sim k_f^{3/2} N^2 M_F^{-1} m^{-2}$. Since $\lambda \sim R^2$ and $\epsilon_{QG} \sim M_F^2$, the critical value scales as $\lambda_c \sim \epsilon_{QG}^{-1/2} N^2 k_f f_0^{-1/2} m^{-2}$. Therefore in figure 9(*b*), we introduce a normalized parameter $\tilde{\lambda} = \lambda(\epsilon_{QG}/\epsilon^0_{QG})^{1/2}$ with $\epsilon^0_{QG} = 8 \times 10^{-5}$ to collapse data with different mean energy injection rates. Hence, we find that the quasilinear dynamics controls the phase transition of the NIW–QG coupled system.

Figure 10 shows the λ dependence of the ratio between the upscale mean energy flux and mean energy injection rate, $\epsilon_{up}/\epsilon_{QG}$. Here, $\epsilon_{up} = \max_{K<k_f} |F_{QG}|$ is the upscale mean energy flux. In figure 10(*a*), we present the results with three mean energy injection rates.

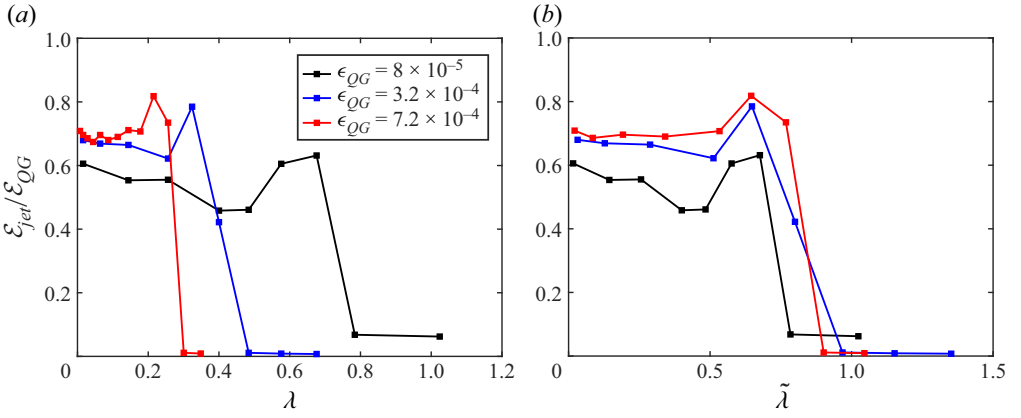

Figure 9. Ratio between jet energy and the QG mean-flow energy with different mean energy injection rates. In (*b*), the horizontal coordinate is normalized as $\tilde{\lambda} = \lambda(\epsilon_{QG}/\epsilon_{QG}^0)^{1/2}$.

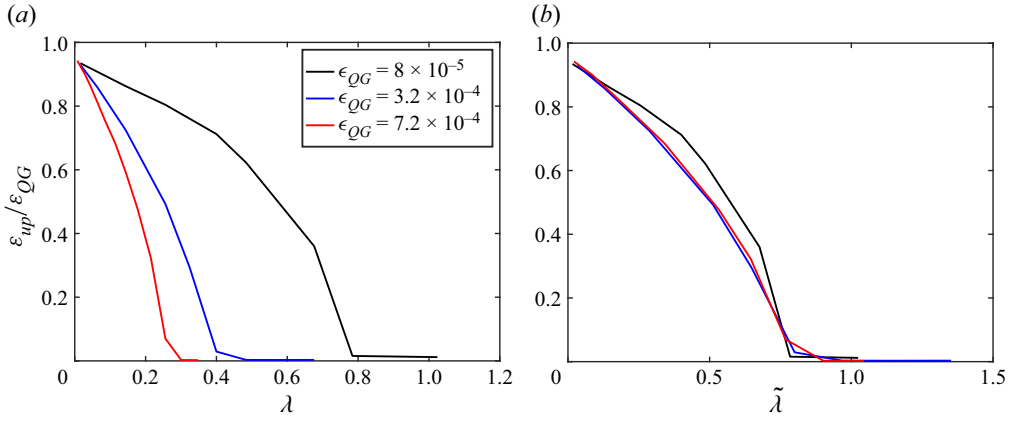

Figure 10. Ratio between the upscale energy flux and the total mean energy injection rate with different mean energy injection rates. In (*b*), the horizontal coordinate is normalized as $\tilde{\lambda} = \lambda(\epsilon_{QG}/\epsilon_{QG}^0)^{1/2}$.

The upscale energy flux ratio gradually decreases as λ increases and finally shows a second-order phase transition across λ_c, which contrasts with the behaviour of $\mathcal{E}_{jet}/\mathcal{E}_{QG}$ shown in figure 9, but these two quantities share the same critical values. This behaviour is similar to that on an f-plane (Xie 2020). Figure 10(*b*) shows that after normalizing λ by $\epsilon_{QG}^{-1/2}$, curves with different mean energy injection rates collapse. This implies that the above-mentioned quasilinear argument controls the phase transition of the NIW–QG coupled system. The concurrence of the disappearance of jet and upscale energy flux implies that we can understand jet annihilation from the perspective of NIW-modified mean energy flux. The injection of NIWs induced downscale flux of mean energy (Xie 2020); therefore, the upscale energy flux decreases and the jets weaken. Thus, from the same perspective, other properties, such as jet spacing, should also be controlled by upscale energy flux, which we study in detail in § 5.

5. Jet spacing

Another important character of jets is their spacing, L_{jet}. We may define L_{jet} from the jet energy spectrum:

$$L_{jet} = \frac{\int E_Z(k)\,\mathrm{d}k}{\int kE_Z(k)\,\mathrm{d}k}. \tag{5.1}$$

Proposed by Rhines (1975), jet spacing can be captured by a characteristic scale $L_{Rh} = \sqrt{U/\beta}$, which is named the Rhines scale. By choosing the r.m.s. of jet velocity, $U_{jet} = \sqrt{2\mathcal{E}_{jet}}$, as the characteristic velocity, the Rhines scale can be expressed as

$$L_{Rh} = \frac{(2\mathcal{E}_{jet})^{1/4}}{\beta^{1/2}}. \tag{5.2}$$

In 2-D β-plane turbulence, energy transfers upscale, and with further frictional damping, the kinetic energy can be obtained from the balance between energy injection and dissipation as $\mathcal{E} = \epsilon/(2\alpha)$ in a statistically steady state. In our system, the QG mean energy transfers bidirectionally. Since the jet is a large-scale structure, one may propose that the upscale energy flux ϵ_{up} is important for jets (cf. Scott & Dritschel 2012). Therefore, following the above-mentioned classic 2-D turbulence argument, we obtain a characteristic scale:

$$L_\alpha = \frac{\epsilon_{up}^{1/4}}{\alpha^{1/4}\beta^{1/2}}. \tag{5.3}$$

We further consider that in the NIW–QG coupled system, QG mean energy flux F_{QG} can be decomposed into the mean part F^m_{QG} and the NIW-related flux F^{NIW}_{QG} (cf. (3.5)). Since a jet is a zonal-mean quantity, we conjecture that only F^m_{QG} is relevant to the jet spacing. Therefore, we propose a characteristic scale estimated by the upscale energy flux induced by mean flow only, $\epsilon_{adv} = \max_{K<k_f} |F^m_{QG}|$:

$$L_{adv} = \frac{\epsilon_{adv}^{1/4}}{\alpha^{1/4}\beta^{1/2}}. \tag{5.4}$$

When no NIWs are injected into the coupled system (i.e. $\lambda = 0$), L_{adv} equals L_α since $\epsilon_{up} = \epsilon_{adv}$.

We show the normalized jet spacing and three normalized characteristic scales in figure 11(a) with λ ranging from 0 to λ_c. As λ increases, jet spacing increases. However, both L_{Rh} and L_α decrease, so they cannot describe jet spacing. Interestingly, even though the presence of NIWs reduces the upscale flux of the mean energy, the jet spacing increases with λ increasing. In contrast, L_{adv} increases as λ increases, which can be seen from the increase of F^m_{QG} (cf. figure 6). Figure 11(b) shows that the jet spacing is well described by L_{adv}, which implies that the upscale energy flux induced by mean advection controls jet formation. Thus, by measuring the mean quantities only, we can capture the jet spacing using the classic Rhines scale as if the NIW is absent, which again points out the catalytic role of NIWs.

6. Near-inertial-wave-induced symmetry breaking

The NIWs break the temporal symmetry by rotating in the direction opposite to that of the background rotation. This temporal symmetry breaking leads to spatial asymmetry, which

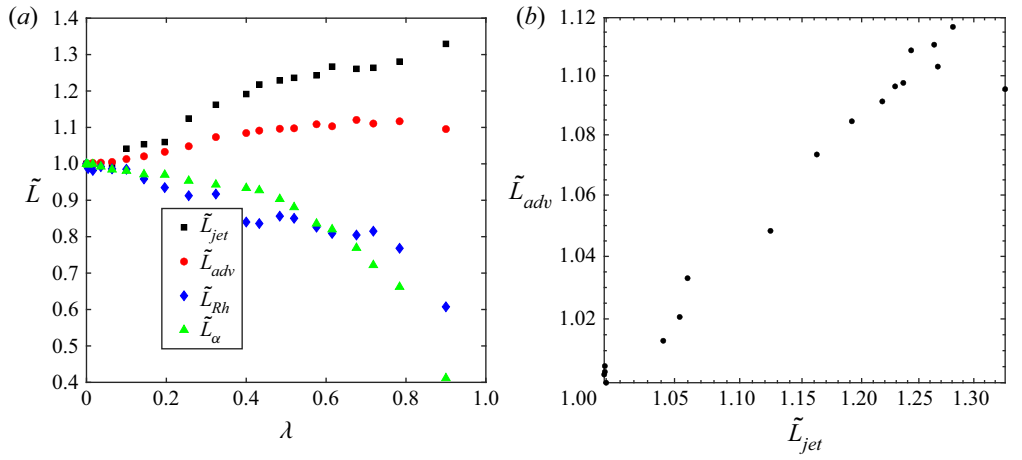

Figure 11. (*a*) Jet spacings and different definitions of Rhines scale with $k_f = 32$, $\epsilon_{QG} = 8 \times 10^{-5}$ and varying λ. The tilde denotes the scale normalized by NIW-free jet spacing ($\lambda = 0$). (*b*) Comparison between the numerically obtained jet spacing $\tilde{L}_{jet}$ and the mean-advection-related Rhines scale $\tilde{L}_{adv}$ with different λ. In these simulations $\epsilon_{QG} = 8 \times 10^{-5}$.

we study in this section from the perspectives of mean-velocity profile and jet meridional migration.

6.1. *Mean-velocity profile*

In this subsection, we focus on the mean-velocity profile of zonal jets. We show the jet velocity profile $\bar{u}$ obtained by taking a zonal average of zonal velocity u in figure 12(*a*). Similar to the classic β-plane jet profile, the zonal velocity has an east–west asymmetry: the east jets have cusps while the west jets are smooth. In figure 12(*a*), the presence of NIWs introduces an additional asymmetry of the jet with steeper left flanks (red rectangles) than the right flanks (blue rectangles). This asymmetry manifests itself in the asymmetric profile of zonal-mean vorticity $\bar{Q} = -\bar{u}_y$ with a greater magnitude of positive vorticity, which is shown in figure 12(*b*). Figure 12(*c*) shows that the zonal-mean wave action $|\bar{\phi}|^2$ concentrates around regions with negative vorticity, $\bar{Q} < 0$, which is consistent with NIW concentration on anticyclones (Kunze 1985; Danioux *et al.* 2015). Since NIWs concentrate on the right flank with negative vorticity, the intensity of NIW–QG interaction there should be more potent than that at the left flank with positive vorticity. The NIW–QG interaction induces a downscale mean-energy flux and increases dissipation at small scales (cf. § 3). Therefore, the mean shear on the left flank is stronger than that on the right flank.

To show the impact of NIW strength on mean-velocity profiles, in figure 13 we compare jet profiles with different λ by moving the profiles to the same peak location. It shows that the asymmetry of jet flanks enhances as λ increases. Since jets are annihilated when $\lambda > \lambda_c$, we only study the jet profile in the parameter regime with $\lambda < \lambda_c$.

To quantify the jet flank asymmetry, we study the skewness of the zonal-mean vorticity $\bar{Q}$. We define $Q_3 = \langle \overline{Q}^3 \rangle$ and $Q_2 = \langle \overline{Q}^2 \rangle$, and use the skewness $S_k = Q_3/Q_2^{3/2}$ to quantify the asymmetry. We present S_k with different ϵ_{QG} and λ in figure 14(*a*). The skewness of the mean vorticity first increases with λ due to NIWs concentrating on the negative vorticity, and then it suddenly drops as λ reaches λ_c because jets are annihilated. Similar to

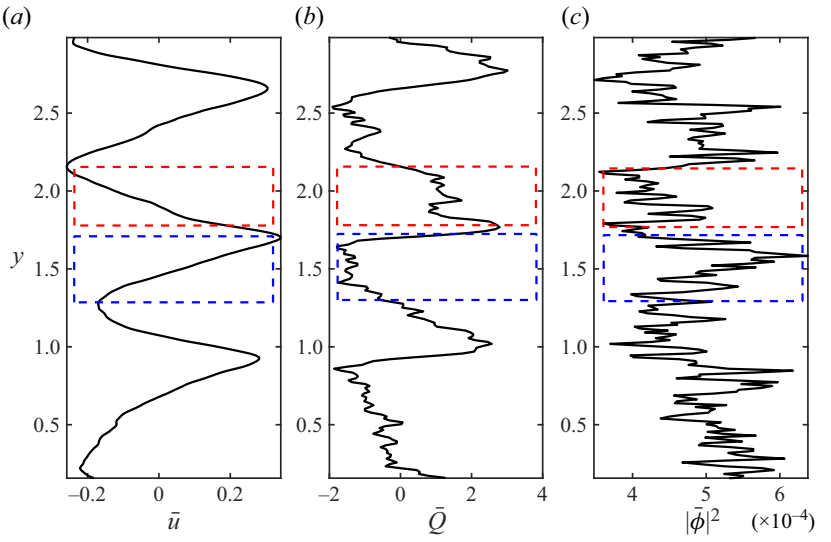

Figure 12. Zonal-mean profiles of (*a*) zonal velocity, (*b*) vorticity and (*c*) wave action with $\epsilon_{QG} = 8 \times 10^{-5}$, $\lambda = 0.4$ at $t = 2000$. The blue and red rectangles denote the regions with positive and negative vorticity, respectively.

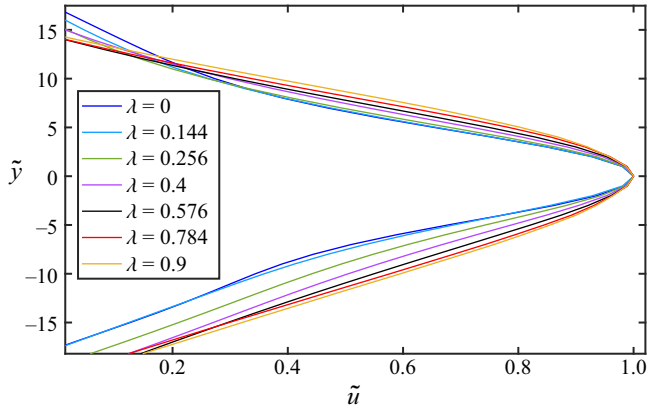

Figure 13. Jet velocity profiles with $\epsilon_{QG} = 8 \times 10^{-5}$ and changing λ. Here, $\tilde{u}$ denotes the moved profiles sharing the same peak location for comparison; $\tilde{y}$ denotes the moved meridional coordinate.

figures 9(*b*) and 10(*b*), figure 14(*b*) shows that the same normalization $\tilde{\lambda} = \lambda(\epsilon_{QG}/\epsilon^0_{QG})^{1/2}$ also works for S_k, which again reveals the significance of quasilinear dynamics (cf. § 4).

Taken together, these results suggest that the mean flow on the right flank is reduced more than that on the left flank due to NIWs concentrating on the right flanks, where anticyclones reside and NIW–mean interaction grows. Therefore, NIWs catalyse the asymmetry of jet flanks. Besides, in the current parameter regime, we find that the Stokes drift (Bühler 2009) is negligible compared with the Lagrangian mean velocity. Details are presented in Appendix A.

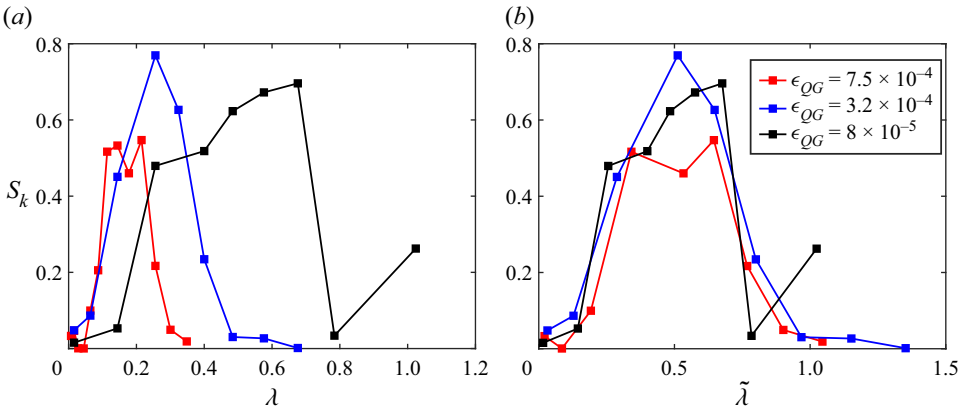

Figure 14. The skewness of zonal-mean vorticity with different mean energy injection rates. In (*b*) the horizontal coordinate is normalized as $\tilde{\lambda} = \lambda(\epsilon_{QG}/\epsilon^0_{QG})^{1/2}$.

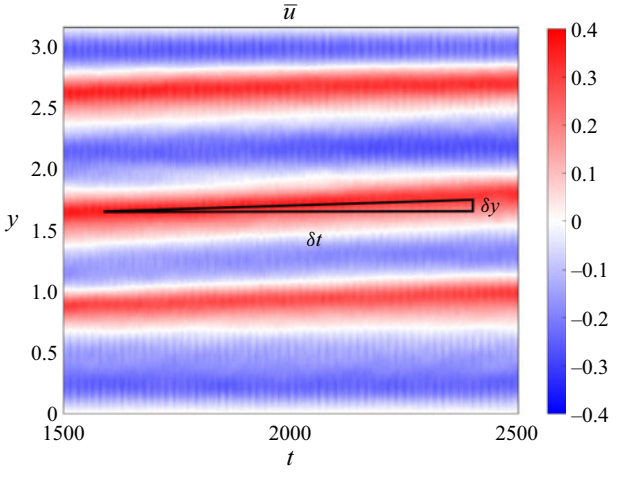

Figure 15. Hovmöller diagram of the zonal-mean zonal velocity with $\epsilon_{QG} = 8 \times 10^{-5}$ and $\lambda = 0.4$.

6.2. *Jet migration*

In this subsection, we focus on the impact of NIWs on jet migration. We show the Hovmöller diagram of the zonal-mean zonal velocity, $\bar{u}$, with $\lambda = 0.4$ and $\epsilon_{QG} = 8 \times 10^{-5}$ in figure 15, where jets migrate with a constant speed in the meridional direction. From this Hovmöller diagram, we can define a jet migration speed $\mathcal{V} = \delta y/\delta t$, where δy is the latitudinal shift and δt is the elapsed time.

Figure 16 shows the dependence of the measured jet migration speed on the energy injection ratio. The zonal jets without NIWs stay static, and as the NIW energy injection rate increases, jet meridional migration speed gradually increases. To find the mechanism behind zonal jet migration, we start from the zonal-mean momentum equation derived from (2.6*a*):

$$\partial_t \bar{u} + \partial_y \overline{u'v'} - \bar{\Lambda} = -\alpha_1 \bar{u} + \nu_1 \frac{\partial^6 \bar{u}}{\partial y^6}, \tag{6.1}$$

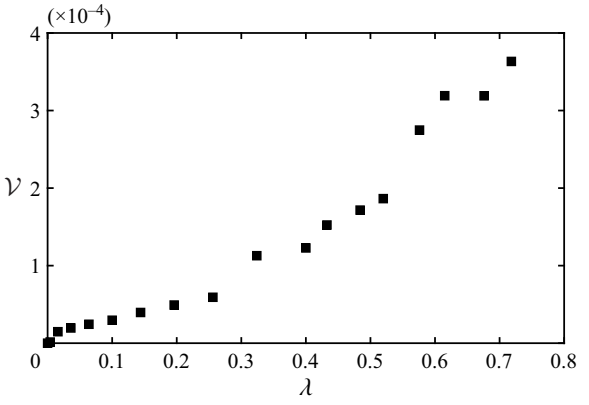

Figure 16. Dependence of jet migration speed $\mathcal{V}$ on λ with $\epsilon_{QG} = 8 \times 10^{-5}$.

where (u', v') is the fluctuation with respect to the zonal-mean velocity (cf. Chemke & Kaspi 2015*b*). Parameter Λ is derived from the wave-related term in (2.10*c*) with $\hat{\Lambda} = -\mathrm{i}\hat{\mathcal{N}}_{NIW}/l$ in Fourier space. Using Taylor's identity

$$-\partial_y(\overline{u'v'}) = \overline{v'Q'}, \tag{6.2}$$

equation (6.1) becomes

$$\partial_t \bar{u} = \overline{v'Q'} + \bar{\Lambda} - \alpha_1 \bar{u} + \nu_1 \frac{\partial^6 \bar{u}}{\partial y^6}. \tag{6.3}$$

Here, $Q' = Q - \bar{Q}$. Assuming that jets migrate in the meridional direction with a constant speed, we consider a frame of reference moving with jets by introducing a coordinate $\varphi = y - \mathcal{V}^* t$ with $\mathcal{V}^*$ the jet migration speed. Thus (6.3) becomes

$$-\mathcal{V}^* \frac{\mathrm{d}\bar{u}}{\mathrm{d}\varphi} = \underbrace{\overline{v'Q'} + \bar{\Lambda} - \alpha_1 \bar{u} + \nu_1 \frac{\partial^6 \bar{u}}{\partial y^6}}_{\mathcal{T}(\varphi)}, \tag{6.4}$$

where we introduce the momentum flux convergence $\mathcal{T}$ for convenience.

In figure 17, we show the NIW-induced asymmetric jet profile (cf. § 6.1) and its corresponding momentum flux convergence $\mathcal{T}$. We define the width of the jet flank as the meridional range with $\bar{u} > 0$, i.e. $\varphi_0^+ - \varphi_0^-$, and φ_{jet} is the latitude of the maximum zonal-mean zonal velocity $\bar{u}_{max}$. Integrating (6.4) from φ_0^- to φ_{jet} and φ_{jet} to φ_0^+ and then subtracting the resultant equations, the jet migration speed $\mathcal{V}^*$ is expressed as

$$\mathcal{V}^* = \frac{1}{2\bar{u}_{max}} \left(\int_{\varphi_{jet}}^{\varphi_0^+} \mathcal{T}\, \mathrm{d}\varphi - \int_{\varphi_0^-}^{\varphi_{jet}} \mathcal{T}\, \mathrm{d}\varphi \right). \tag{6.5}$$

To find the dominant effect on jet migration, we introduce the following decomposition:

$$\int_{\varphi_{jet}}^{\varphi_0^+} \mathcal{T}\, \mathrm{d}\varphi - \int_{\varphi_0^-}^{\varphi_{jet}} \mathcal{T}\, \mathrm{d}\varphi = \mathcal{I}_{adv} + \mathcal{I}_{NIW} + \mathcal{I}_{\alpha} + \mathcal{I}_{\nu}, \tag{6.6}$$

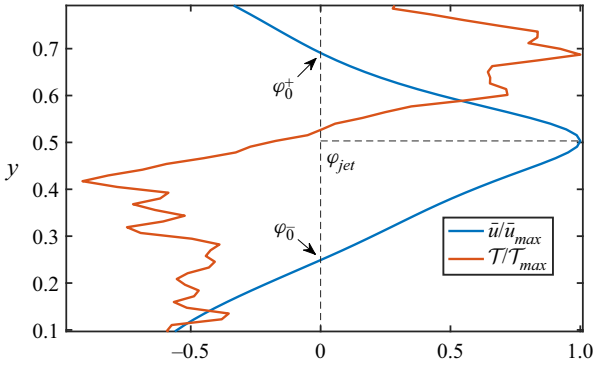

Figure 17. Profiles of the normalized zonal-mean velocity $\bar{u}/\bar{u}_{max}$ and the normalized momentum flux convergence $\mathcal{T}/\mathcal{T}_{max}$ with $\epsilon_{QG} = 8 \times 10^{-5}$ and $\lambda = 0.4$.

where

$$\mathcal{I}_{adv} = \int_{\varphi_{jet}}^{\varphi_0^+} \overline{v'Q'}\,\mathrm{d}\varphi - \int_{\varphi_0^-}^{\varphi_{jet}} \overline{v'Q'}\,\mathrm{d}\varphi, \tag{6.7a}$$

$$\mathcal{I}_{NIW} = \int_{\varphi_{jet}}^{\varphi_0^+} \bar{\Lambda}\,\mathrm{d}\varphi - \int_{\varphi_0^-}^{\varphi_{jet}} \bar{\Lambda}\,\mathrm{d}\varphi, \tag{6.7b}$$

$$\mathcal{I}_{\alpha} = \int_{\varphi_{jet}}^{\varphi_0^+} -\alpha_1 \bar{u}\,\mathrm{d}\varphi + \int_{\varphi_0^-}^{\varphi_{jet}} \alpha_1 \bar{u}\,\mathrm{d}\varphi, \tag{6.7c}$$

$$\mathcal{I}_{\nu} = \int_{\varphi_{jet}}^{\varphi_0^+} \nu_1 \frac{\partial^6 \bar{u}}{\partial \varphi^6}\,\mathrm{d}\varphi - \int_{\varphi_0^-}^{\varphi_{jet}} \nu_1 \frac{\partial^6 \bar{u}}{\partial \varphi^6}\,\mathrm{d}\varphi. \tag{6.7d}$$

Figure 18(*a*) shows the λ dependence of these terms. We observe that the total net momentum flux, $\mathcal{I}_{total} = \mathcal{I}_{adv} + \mathcal{I}_{NIW} + \mathcal{I}_{\alpha} + \mathcal{I}_{\nu}$, increases with λ. Therein, the dissipation-related net momentum fluxes, $\mathcal{I}_{\alpha}$ and $\mathcal{I}_{\nu}$, are negligible. The advection-related net momentum flux, $\mathcal{I}_{adv}$, is dominant and increases with λ, while the wave-related net momentum flux, $\mathcal{I}_{NIW}$, has an opposite sign to $\mathcal{I}_{total}$ and therefore prohibits jet migration. Figure 18(*b*) shows that when λ ranges from 0 to λ_c, the jet migration speeds calculated from (6.5) capture the migration speeds obtained from numerical simulations. The impact of NIWs on jet migration again shows its catalytic effect – the direct effect of NIWs, $\mathcal{I}_{NIW}$, restrains jet migration, but NIW-modified mean flow dominates and drives the migration.

The direction of jet migration can be understood as a consequence of NIW concentration in anticyclones (Danioux *et al.* 2015). Since NIWs accumulate in anticyclones, more energy is transferred downscale by negative vorticity and finally dissipates (cf. § 3), so the negative vorticity of the mean flow is weaker than the positive vorticity. Then the vortex pairs propagate poleward. This phenomenon was observed in simulations of both primitive equations (Hernandez-Duenas, Smith & Stechmann 2014) and reduced model (Xie & Vanneste 2015). Similarly, figure 19 shows that both jets and waves migrate poleward and NIWs concentrate in regions with negative vorticity, so jets migrate poleward.

We need to note that the coupled model was initially derived in the ocean context. But most jets in ocean models are found to propagate equatorward (Chan *et al.* 2007;

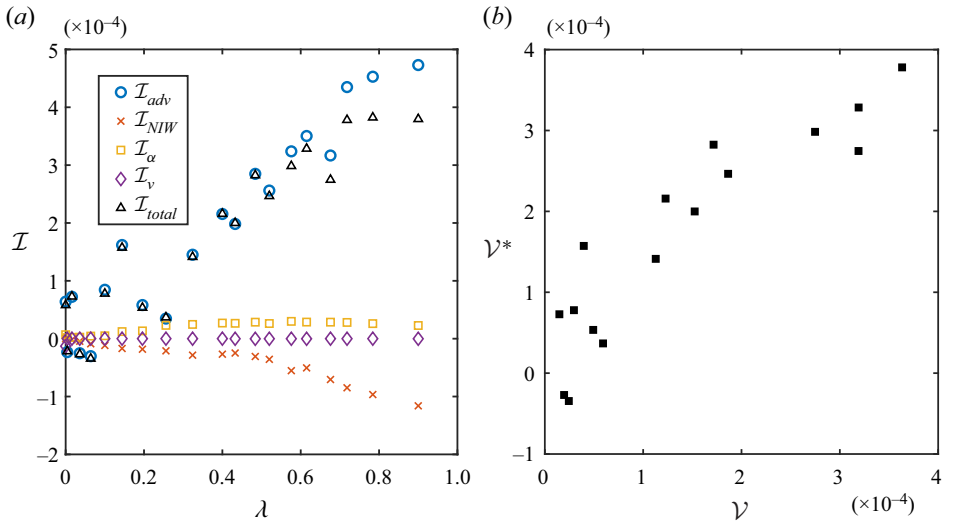

Figure 18. (*a*) The dependences of the net momentum flux $\mathcal{I}$ on λ. (*b*) Numerically obtained jet migration speed $\mathcal{V}$ against the migration speed $\mathcal{V}^*$ calculated from momentum balance (6.5). Here, $\epsilon_{QG} = 8 \times 10^{-5}$.

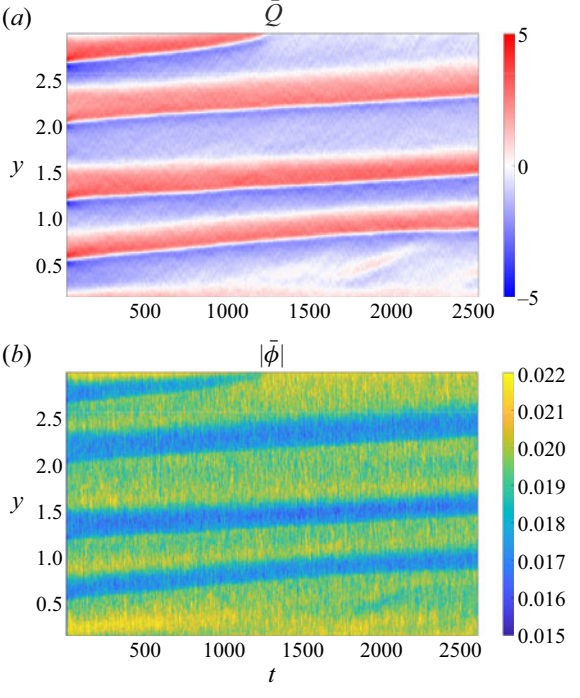

Figure 19. Hovmöller diagram of the zonal-mean (*a*) vorticity and (*b*) NIW amplitude with $\epsilon_{QG} = 8 \times 10^{-5}$ and $\lambda = 0.4$.

Ashkenazy & Tziperman 2016). Nevertheless, poleward migration was also observed over a short range and less systematically (Chan *et al.* 2007). Thus, the impact of NIWs cannot fully explain the migration of oceanic jets.

7. Summary and discussion

Using a 2-D single-vertical-mode NIW–QG coupled model on a β-plane (2.1), we study the impact of NIWs on zonal jets in forced-dissipative statistically steady states. We explore the parameter regime with different mean energy injection rates and the ratio between NIW and QG mean energy injection rate, which λ parametrizes.

The presence of NIWs leads to bidirectional mean-flow energy transfer, which shows a second-order phase transition with a critical value λ_c. When $0 < \lambda < \lambda_c$, the energy of balanced flow transfers to both large and small scales. As λ increases, the portion of upscale transferring energy decreases, while the proportion of zonal-jet energy in the energy of the balanced flow remains almost unchanged. When $\lambda > \lambda_c$, the QG inverse cascade is eliminated and zonal jets cannot form. Since there is a negligible energy exchange between mean flows and NIWs, the existence of the catalytic wave induction mechanism initially proposed on an f-plane (Xie 2020) is justified on a β-plane. This mechanism differs from the spontaneous and stimulated loss of balance (Vanneste 2013; Xie & Vanneste 2015), where the mean energy converts to that of NIWs and finally dissipates.

Based on the picture that the β-effect arrests the upscale energy flux, previous studies (Rhines 1975; Williams 1978) showed that the Rhines scale could capture the zonal jet spacing. Nevertheless, we find that the Rhines scale calculated from the r.m.s. velocity (Rhines 1975) and the upscale energy transfer rate ϵ_{up} (Vallis 2006) cannot sufficiently describe jet spacing when NIWs are present. Instead, the Rhines scale calculated from the upscale-mean-energy transfer rate induced by the mean advection, $L_{adv} = (2\epsilon_{adv})^{1/4}\alpha^{-1/4}\beta^{-1/2}$, captures the jet spacing before jet total annihilation by NIWs.

The concentration of NIWs in anticyclones induces symmetry breaking of zonal jets. The NIWs lead to an asymmetry of the left and right flanks about the jet profile cusp, where the right flank's slope is flatter than that of the left flank. Moreover, this asymmetry enhances as the energy injection ratio λ increases. The concentration of NIWs in anticyclones or regions with negative vorticity (Danioux *et al.* 2015) can explain the mechanism behind such asymmetry. Therefore at the right flank of a jet cusp, stronger NIW–mean flow interaction leads to stronger downscale mean energy flux induced by waves, which enhances the mean flow dissipation, so the right flank is flatter than the left flank. The NIW-induced symmetry breaking also manifests in jets' poleward migration. The interaction between NIWs and mean flows also influences the jet migration speed in the meridional direction. Based on an expression of migration speed calculated from the momentum equation in a frame of reference moving with jets (Chemke & Kaspi 2015*b*), we find that the distribution of the momentum flux convergence to the cusps in the velocity profile is asymmetric, which leads to jet migration. In this expression, the mean-advection net momentum flux dominates, while the NIW-related term impedes jet migration but is of secondary importance. Furthermore, we numerically find that the migration speed increases as the energy injection of NIWs increases. Even though the asymmetric jet profile and meridional migration coexist, we do not know if this coexistence is inevitable. Such coexistence is also observed in jet migration without wave impact (cf. Cope 2020), so there is more to be understood on jet asymmetry.

Considering that the strong vortex regions are close to the peak of the cusp of eastward jets, this poleward migration mimics the left turning of vortex dipoles (Hernandez-Duenas *et al.* 2014; Xie & Vanneste 2015). Even though the reduced model is derived in an oceanic context (Xie & Vanneste 2015), the jet migration direction coincides with the results of observations (Riehl *et al.* 1950; Dickey *et al.* 1992) and numerical simulations (James &

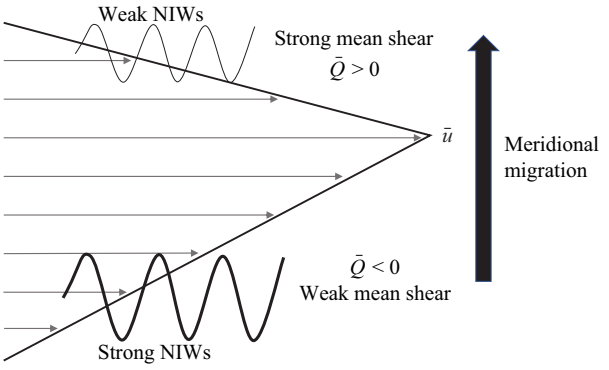

Figure 20. Illustration of the jet–NIW interaction.

Dodd 1996; Chemke & Kaspi 2015*b*) in the atmosphere. However, in the ocean, poleward migration of zonal flow is observed less frequently (Chan *et al.* 2007), implying that the impact of NIWs on zonal jets may not be a dominant effect that determines the direction of oceanic jet migration.

The catalytic wave impact on zonal jets manifests itself from three aspects. (i) In the mean-flow bidirectional energy transfer across scales, NIWs impact the relative strength of the downscale flux without energy conversion between NIW and mean flow. (ii) The jet spacing is described by the Rhines scale obtained from the upscale mean energy flux induced by mean flow alone as if there is no NIW. (iii) The jet meridional migration speed is dominated by the asymmetry of mean momentum flux induced by mean flow, but in our set-up, this asymmetry is induced by NIWs. We summarize the effects of NIW concentration on the right flank, the asymmetry of the jet and the meridional migration in figure 20. However, we do not understand why these wave effects are catalytic, which is an interesting future direction.

We close this paper by pointing out several limitations of the present study. To solve the coupled NIW–QG model with the pseudospectral method, we prescribe a periodic $\beta(y)$ (cf. 2.4). Therefore, around one-half of the meridional extension approximates a β-plane, while other regions are only introduced to construct a periodic domain for the spectral method. To avoid the Gibbs effect, the β-effect is artificially prescribed with a narrow but finite range of non-constant value, which leads to unphysical effects, but we assume that this effect is only confined in this narrow region, which is the drawback of this set-up. In addition, the NIW–QG model in this paper is asymptotically derived in the regime of small Rossby and small Burger numbers (cf. Xie & Vanneste 2015), which limits the validity of the current results; therefore, it would be interesting to check if our results persist in primitive equations in future work. Besides, we applied a simple turbulence phenomenology based on energy flux to explain jet formation, but we did not distinguish the local and non-local effects in spectral space. So in future work, we plan to study the impact of waves on jets by applying a quasilinear approximation to the balanced motion (cf. Marston & Tobias 2023).

Funding. The authors gratefully acknowledge financial support from the National Natural Science Foundation of China (NSFC) under grant nos. 92052102 and 12272006 and Joint Laboratory of Marine Hydrodynamics and Ocean Engineering, Pilot National Laboratory for Marine Science and Technology (Qingdao) under grant no. 2022QNLM010201.

Declaration of interests. The authors report no conflict of interest.

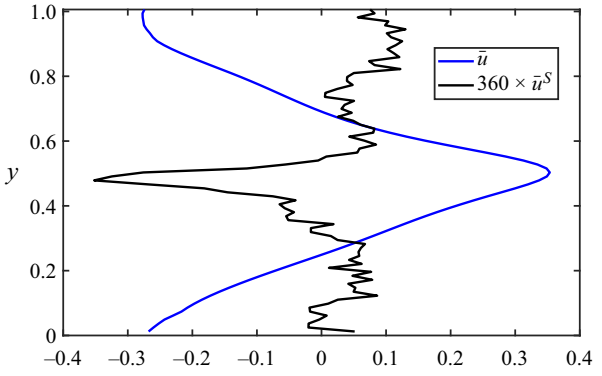

Figure 21. The Lagrangian mean velocity profile $\bar{u}$ and the Stokes drift $\bar{u}^S$ with $\epsilon_{QG} = 8 \times 10^{-5}$ and $R = 2.0$.

Author ORCIDs.
Lin-Fan Zhang https://orcid.org/0000-0001-5853-4118;
Jin-Han Xie https://orcid.org/0000-0003-0502-8662.

Appendix A. Stokes drift

The vertical plane-wave displacement and velocity are expressed by the complex amplitude ϕ as

$$\xi + \mathrm{i}\eta = \phi\, \mathrm{e}^{-\mathrm{i}f_0 t + \mathrm{i}mz}, \quad \zeta = \frac{\mathrm{i}}{m}\phi_s\, \mathrm{e}^{-\mathrm{i}f_0 t + \mathrm{i}mz} + \text{c.c.} \tag{A1a,b}$$

and

$$u_0 + \mathrm{i}v_0 = -\mathrm{i}f_0\phi\, \mathrm{e}^{-\mathrm{i}f_0 t + \mathrm{i}mz}, \quad w_0 = \frac{f_0}{m}\phi_s\, \mathrm{e}^{-\mathrm{i}f_0 t + \mathrm{i}mz} + \text{c.c.}, \tag{A2a,b}$$

where $s = x + \mathrm{i}y$, $\partial_s = (\partial_x - \mathrm{i}\partial_y)/2$ and 'c.c.' denotes the complex conjugate. The Lagrangian mean velocity differs from the Eulerian mean velocity by a Stokes drift (Bühler 2009), which is expressed as

$$\bar{\boldsymbol{u}}^S = \overline{\boldsymbol{\xi} \cdot \boldsymbol{\nabla} \boldsymbol{u}_0}. \tag{A3}$$

To check the difference between the Lagrangian and Eulerian mean velocity, we calculate the Stokes drift by substituting (A1*a*,*b*) and (A2*a*,*b*) into (A3):

$$\bar{\boldsymbol{u}}^S = \left(-\frac{f_0}{2}\nabla^\perp |\phi|^2, \frac{f_0}{4m}(\phi^* \Delta\phi + \text{c.c.}) + \frac{f_0}{2m}[|\phi_y|^2 + |\phi_x|^2 + \mathrm{i}(\phi_x \phi_y^* - \text{c.c.})] \right). \tag{A4}$$

Here, wave action acts as the streamfunction of the horizontal components of Stokes drift (Rocha *et al.* 2018). Since NIWs concentrate in regions with negative vorticity (Danioux *et al.* 2015), the perpendicular gradient of wave action is large at the peak of the mean velocity profile. Therefore, Stokes drift peaks around the maximum Lagrangian mean velocity. In figure 21, the Stokes drift is much weaker than the Lagrangian mean flow, so in the main text we do not pay special attention to the Eulerian mean velocity.

References

Abernathey, R., Marshall, J. & Ferreira, D. 2011 The dependence of southern ocean meridional overturning on wind stress. *J. Phys. Oceanogr.* **41** (12), 2261–2278.

ANDREWS, D.G. & MCINTYRE, M.E. 1978 An exact theory of nonlinear waves on a Lagrangian-mean flow. *J. Fluid Mech.* **89** (4), 609–646.

ASHKENAZY, Y. & TZIPERMAN, E. 2016 Variability, instabilities, and eddies in a snowball ocean. *J. Clim.* **29** (2), 869–888.

ASSELIN, O., THOMAS, L.N., YOUNG, W.R. & RAINVILLE, L. 2020 Refraction and straining of near-inertial waves by barotropic eddies. *J. Phys. Oceanogr.* **50**, 3439–3454.

ASSELIN, O. & YOUNG, W.R. 2019 An improved model of near-inertial wave dynamics. *J. Fluid Mech.* **876**, 428–448.

ASSELIN, O. & YOUNG, W.R. 2020 Penetration of wind-generated near-inertial waves into a turbulent ocean. *J. Phys. Oceanogr.* **50** (6), 1699–1716.

BARKAN, R., SRINIVASAN, K., YANG, L., MCWILLIAMS, J.C., GULA, J. & VIC, C. 2021 Oceanic mesoscale eddy depletion catalyzed by internal waves. *Geophys. Res. Lett.* **48**, e2021GL094376.

BARKAN, R., WINTERS, K.B. & MCWILLIAMS, J.C. 2017 Stimulated imbalance and the enhancement of eddy kinetic energy dissipation by internal waves. *J. Phys. Oceanogr.* **47** (1), 181–198.

BERLOFF, P., KAMENKOVICH, I. & PEDLOSKY, J. 2009 A mechanism of formation of multiple zonal jets in the oceans. *J. Fluid Mech.* **628**, 395–425.

BOUCHET, F., MARSTON, J.B. & TANGARIFE, T. 2018 Fluctuations and large deviations of reynolds stresses in zonal jet dynamics. *Phys. Fluids* **30** (1), 015110.

BOUCHET, F., ROLLAND, J. & SIMONNET, E. 2019 Rare event algorithm links transitions in turbulent flows with activated nucleations. *Phys. Rev. Lett.* **122** (7), 074502.

BOUCHET, F. & VENAILLE, A. 2012 Statistical mechanics of two-dimensional and geophysical flows. *Phys. Rep.* **515** (5), 227–295.

BÜHLER, O. 2009 *Waves and Mean Flows*. Cambridge University Press.

CHAN, C.J., PLUMB, R.A. & CEROVECKI, I. 2007 Annular modes in a multiple migrating zonal jet regime. *J. Atmos. Sci.* **64** (11), 4053–4068.

CHEKHLOV, A., ORSZAG, S.A., SUKORIANSKY, S., GALPERIN, B. & STAROSELSKY, I. 1996 The effect of small-scale forcing on large-scale structures in two-dimensional flows. *Phys.* D **98** (2-4), 321–334.

CHEMKE, R. & KASPI, Y. 2015*a* The latitudinal dependence of atmospheric jet scales and macroturbulent energy cascades. *J. Atmos. Sci.* **72** (10), 3891–3907.

CHEMKE, R. & KASPI, Y. 2015*b* Poleward migration of eddy-driven jets: poleward migration of eddy-driven jets. *J. Adv. Model. Earth Syst.* **7** (3), 1457–1471.

COPE, L. 2020 The dynamics of geophysical and astrophysical turbulence. PhD Thesis, University of Cambridge.

COX, S.M. & MATTHEWS, P.C. 2002 Exponential time differencing for stiff systems. *J. Comput. Phys.* **176** (2), 430–455.

DANILOV, S.D. & GURARIE, D 2000 Quasi-two-dimensional turbulence. *Phys. Uspekhi* **43** (9), 863–900.

DANILOV, S. & GURARIE, D. 2004 Scaling, spectra and zonal jets in beta-plane turbulence. *Phys. Fluids* **16** (7), 2592–2603.

DANIOUX, E., VANNESTE, J. & BÜHLER, O. 2015 On the concentration of near-inertial waves in anticyclones. *J. Fluid Mech.* **773**, R2.

DANIOUX, E., VANNESTE, J., KLEIN, P. & SASAKI, H. 2012 Spontaneous inertia-gravity-wave generation by surface-intensified turbulence. *J. Fluid Mech.* **699**, 153–173.

DICKEY, J.O., MARCUS, S.L. & HIDE, R. 1992 Global propagation of interannual fluctuations in atmospheric angular momentum. *Nature* **357** (6378), 484–488.

DRITSCHEL, D.G. & MCINTYRE, M.E. 2008 Multiple jets as PV staircases: the phillips effect and the resilience of eddy-transport barriers. *J. Atmos. Sci.* **65** (3), 855–874.

DUNKERTON, T.J. & SCOTT, R.K. 2008 A barotropic model of the angular momentum–conserving potential vorticity staircase in spherical geometry. *J. Atmos. Sci.* **65** (4), 1105–1136.

ELIPOT, S., LUMPKIN, R. & PRIETO, G. 2010 Modification of inertial oscillations by the mesoscale eddy field. *J. Geophys. Res.* **115**, C09010.

FARRELL, B.F. & IOANNOU, P.J. 2003 Structural stability of turbulent jets. *J. Atmos. Sci.* **60** (17), 2101–2118.

FELDSTEIN, S.B. 1998 An observational study of the intraseasonal poleward propagation of zonal mean flow anomalies. *J. Atmos. Sci.* **55** (15), 2516–2529.

FERRARI, R. & WUNSCH, C. 2009 Ocean circulation kinetic energy: reservoirs, sources, and sinks. *Annu. Rev. Fluid Mech.* **41** (1), 253–282.

FU, L.-L. 1981 Observations and models of inertial waves in the deep ocean. *Rev. Geophys. Space Phys.* **19** (1), 141–170.

GALPERIN, B. & READ, P.L. (Eds.) 2019 *Zonal Jets: Phenomenology, Genesis, and Physics*, 1st edn. Cambridge University Press.

GALPERIN, B., SUKORIANSKY, S. & DIKOVSKAYA, N. 2010 Geophysical flows with anisotropic turbulence and dispersive waves: flows with a β-effect. *Ocean Dyn.* **60** (2), 427–441.

GALPERIN, B., SUKORIANSKY, S., DIKOVSKAYA, N., READ, P.L., YAMAZAKI, Y.H. & WORDSWORTH, R. 2006 Anisotropic turbulence and zonal jets in rotating flows with a β-effect. *Nonlinear Process. Geophys.* **13** (1), 83–98.

GARCÍA-MELENDO, E. 2001 A study of the stability of Jovian zonal winds from HST images: 1995–2000. *Icarus* **152** (2), 316–330.

GERTZ, A. & STRAUB, D.N. 2009 Near-inertial oscillations and the damping of midlatitude gyres: a modeling study. *J. Phys. Oceanogr.* **39** (9), 2338–2350.

GRISOUARD, N. & THOMAS, L.N. 2016 Energy exchanges between density fronts and near-inertial waves reflecting off the ocean surface. *J. Phys. Oceanogr.* **46** (2), 501–516.

HERNANDEZ-DUENAS, G., SMITH, L.M. & STECHMANN, S.N. 2014 Investigation of Boussinesq dynamics using intermediate models based on wave–vortical interactions. *J. Fluid Mech.* **747**, 247–287.

JAMES, I.N. & DODD, J.P. 1996 A mechanism for the low-frequency variability of the mid-latitude troposphere. *Q. J. R. Meteorol. Soc.* **122** (533), 1197–1210.

JOYCE, T.M., TOOLE, J.M., KLEIN, P. & THOMAS, L.N. 2013 A near-inertial mode observed within a gulf stream warm-core ring. *J. Geophys. Res. Oceans* **118** (4), 1797–1806.

KAFIABAD, H.A., VANNESTE, J. & YOUNG, W.R. 2021 Interaction of near-inertial waves with an anticyclonic vortex. *J. Phys. Oceanogr.* **51**, 2035–2048.

KRAICHNAN, R.H. 1967 Inertial ranges in two-dimensional turbulence. *Phys. Fluids* **10** (7), 1417–1423.

KUNZE, E. 1985 Near-inertial wave propagation in geostrophic shear. *J. Phys. Oceanogr.* **15** (5), 544–565.

KUNZE, E., SCHMITT, R.W. & TOOLE, J.M. 1995 The energy balance in a warm-core ring's near-inertial critical layer. *J. Phys. Oceanogr.* **25** (5), 942–957.

LEE, D.-K. & NIILER, P.P. 1998 The inertial chimney: the near-inertial energy drainage from the ocean surface to the deep layer. *J. Geophys. Res.: Oceans* **103** (C4), 7579–7591.

LEMASQUERIER, D., FAVIER, B. & LE BARS, M. 2021 Zonal jets at the laboratory scale: hysteresis and Rossby waves resonance. *J. Fluid Mech.* **910**, A18.

LIGHTHILL, J. 1978 *Waves in Fluids*. Cambridge University Press.

MALTRUD, M.E. & VALLIS, G.K. 1991 Energy spectra and coherent structures in forced two-dimensional and beta-plane turbulence. *J. Fluid Mech.* **228**, 321–342.

MANFROI, A.J. & YOUNG, W.R. 1999 Slow evolution of zonal jets on the beta plane. *J. Atmos. Sci.* **56** (5), 784–800.

MARCUS, P.S. & LEE, C. 1998 A model for eastward and westward jets in laboratory experiments and planetary atmospheres. *Phys. Fluids* **10** (6), 1474–1489.

MARSTON, J.B. & TOBIAS, S.M. 2023 Recent developments in theories of inhomogeneous and anisotropic turbulence. *Annu. Rev. Fluid Mech.* **55** (1), 351–375.

NAGAI, T., TANDON, A., KUNZE, E. & MAHADEVAN, A. 2015 Spontaneous generation of near-inertial waves by the kuroshio front. *J. Phys. Oceanogr.* **45** (9), 2381–2406.

OKUNO, A. & MASUDA, A. 2003 Effect of horizontal divergence on the geostrophic turbulence on a beta-plane: suppression of the Rhines effect. *Phys. Fluids* **15** (1), 56–65.

PLOUGONVEN, R. & SNYDER, C. 2007 Inertia–gravity waves spontaneously generated by jets and fronts. Part I: different baroclinic life cycles. *J. Atmos. Sci.* **64**, 2502–2520.

RHINES, P.B. 1975 Waves and turbulence on a beta-plane. *J. Fluid Mech.* **69** (3), 417–443.

RHINES, P.B. 1979 Geostrophic turbulence. *Annu. Rev. Fluid Mech.* **11**, 401–441.

RHINES, P.B. 1994 Jets. *Chaos* **4** (2), 313–339.

RIEHL, H., YEH, T.C. & LA SEUR, N.E. 1950 A study of variations of the general circulation. *J. Meteorol.* **7** (3), 181–194.

ROCHA, C.B., WAGNER, G.L. & YOUNG, W.R. 2018 Stimulated generation: extraction of energy from balanced flow by near-inertial waves. *J. Fluid Mech.* **847**, 417–451.

ROLLAND, J. & SIMONNET, E. 2015 Statistical behaviour of adaptive multilevel splitting algorithms in simple models. *J. Comput. Phys.* **283**, 541–558.

SALMON, R. 2013 An alternative view of generalized Lagrangian mean theory. *J. Fluid Mech.* **719**, 165–182.

SANCHEZ-LAVEGA, A. & ROJAS, J.F. 2000 Saturn's zonal winds at cloud level. *Icarus* **147** (2), 405–420.

SÁNCHEZ-LAVEGA, A., *et al.* 2008 Depth of a strong jovian jet from a planetary-scale disturbance driven by storms. *Nature* **451** (7177), 437–440.

SCOTT, R.K. & DRITSCHEL, D.G. 2012 The structure of zonal jets in geostrophic turbulence. *J. Fluid Mech.* **711**, 576–598.

SHAKESPEARE, C.J. & MCC. HOGG, A. 2018 The life cycle of spontaneously generated internal waves. *J. Phys. Oceanogr.* **48** (2), 343–359.
SMITH, K.S. 2004 A local model for planetary atmospheres forced by small-scale convection. *J. Atmos. Sci.* **61** (12), 1420–1433.
SMITH, L.M. & WALEFFE, F. 2002 Generation of slow large scales in forced rotating stratified turbulence. *J. Fluid Mech.* **451**, 145–168.
SOWARD, A.M. & ROBERTS, P.H. 2010 The hybrid Euler–Lagrange procedure using an extension of Moffatt's method. *J. Fluid Mech.* **661**, 45–72.
SRINIVASAN, K. & YOUNG, W.R. 2012 Zonostrophic instability. *J. Atmos. Sci.* **69** (5), 1633–1656.
SUKORIANSKY, S., DIKOVSKAYA, N. & GALPERIN, B. 2007 On the arrest of inverse energy cascade and the rhines scale. *J. Atmos. Sci.* **64** (9), 3312–3327.
TAYLOR, S. & STRAUB, D. 2016 Forced near-inertial motion and dissipation of ow-frequency kinetic energy in a wind-driven channel flow. *J. Phys. Oceanogr.* **46** (1), 79–93.
THOMAS, L.N. 2012 On the effects of frontogenetic strain on symmetric instability and inertia–gravity waves. *J. Fluid Mech.* **711**, 620–640.
THOMAS, J. & ARUN, S. 2020 Near-inertial waves and geostrophic turbulence. *Phys. Rev. Fluid* **5** (1), 014801.
THOMAS, L.N., RAINVILLE, L., ASSELIN, O., YOUNG, W.R., GIRTON, J., WHALEN, C.B., CENTURIONI, L. & HORMANN, V. 2020 Direct observations of near-inertial wave ζ -refraction in a dipole vortex. *Geophys. Res. Lett.* **47**, e2020GL090375.
UPPALA, S.M., *et al.* 2005 The ERA-40 re-analysis. *J. Atmos. Sci.* **131** (612), 2961–3012.
VALLIS, G.K. 2006 *Atmospheric and Oceanic Fluid Dynamics*. Cambridge University Press.
VALLIS, G.K. & MALTRUD, M. 1993 Generation of mean flows and jets on a beta plane and over topography. *J. Phys. Oceanogr.* **23**, 1346–1362.
VANNESTE, J. 2008 Exponential smallness of inertia–gravity wave generation at small Rossby number. *J. Atmos. Sci.* **65**, 1622–1637.
VANNESTE, J. 2013 Balance and spontaneous wave generation in geophysical flows. *Annu. Rev. Fluid Mech.* **45** (1), 147–172.
VASAVADA, A.R. & SHOWMAN, A.P. 2005 Jovian atmospheric dynamics: an update after *Galileo* and *Cassini*. *Rep. Prog. Phys.* **68** (8), 1935–1996.
WAGNER, G.L. & YOUNG, W.R. 2016 A three-component model for the coupled evolution of near-inertial waves, quasi-geostrophic flow and the near-inertial second harmonic. *J. Fluid Mech.* **802**, 806–837.
WHITT, D.B. & THOMAS, L.N. 2015 Resonant generation and energetics of wind-forced near-inertial motions in a geostrophic flow. *J. Phys. Oceanogr.* **45**, 181–208.
WILLIAMS, G.P. 1978 Planetary circulations: 1. Barotropic representation of jovian and terrestrial turbulence. *J. Atmos. Sci.* **35** (8), 1399–1426.
WILLIAMS, G.P. 2003 Jovian dynamics. Part III: multiple, migrating, and equatorial jets. *J. Atmos. Sci.* **60** (10), 1270–1296.
WOILLEZ, E. & BOUCHET, F. 2019 Barotropic theory for the velocity profile of Jupiter's turbulent jets: an example for an exact turbulent closure. *J. Fluid Mech.* **860**, 577–607.
XIE, J.-H. 2020 Downscale transfer of quasigeostrophic energy catalyzed by near-inertial waves. *J. Fluid Mech.* **904**, A40.
XIE, J.-H. & VANNESTE, J. 2015 A generalised-Lagrangian-mean model of the interactions between near-inertial waves and mean flow. *J. Fluid Mech.* **774**, 143–169.
YOUNG, W. & BEN JELLOUL, M. 1997 Propagation of near-inertial oscillations through a geostrophic flow. *J. Mar. Res.* **55**, 735–766.
ZEITLIN, V. 2008 Decoupling of balanced and unbalanced motions and inertia–gravity wave emission: small versus large Rossby numbers. *J. Atmos. Sci.* **65**, 3528–354.